UNIVERSITÀ DEGLI STUDI DI MILANO

Scuola di Dottorato in Fisica, Astrofisica e Fisica Applicata

37° Ciclo

The Spinterface Problem: ab-initio studies of Fe-phthalocyanine on Transition-Metal Oxides

Settore Scientifico Disciplinare FIS/04

Supervisore: Professor Guido Fratesi
Co-supervisore: Dottoressa Simona Achilli

Coordinatore: Professor Aniello Mennella

Tesi di Dottorato di:
Marco Marino

Anno Accademico 2023-2024

Commission of the final examination:

External Referees:
Prof. Matteo Cococcioni, University of Pavia, Pavia, Italy

Prof. Peter Puschnig, University of Graz, Graz, Austria

External Members:
Prof. Matteo Cococcioni, University of Pavia, Pavia, Italy

Prof. Peter Puschnig, University of Graz, Graz, Austria

Internal Member:
Prof. Giovanni Onida, University of Milan, Milan, Italy

Final examination:

Date 22/11/2024

University of Milan, Department of Physics, Milan, Italy

To my family

Contents

List of Figures

List of Tables

Synopsis

Motivation

In organic spintronics, the problem of understanding the interfaces of organic-inorganic heterostructures is acquiring major interest, so to coin the term spinterface. In our research, as part of the EU project SINFONIA (European Union's Horizon 2020 Research and Innovation program under grant agreement no. 964396 FET-Open SINFONIA), that funded my PhD scholarship and which will be described in more detail in section 1.7, we attempted to understand how the spinterfaces can be used in antiferromagnetic spintronics devices. In particular, the adsorption of organic molecules on antiferromagnetic substrates offers a channel to modify the magnetic properties of the substrates through light, without the need of a strong spin-orbit coupling and consequent effect on the spin transport properties.

Thesis overview

Transition-metal oxides are optimal candidates as antiferromagnetic and low spin-orbit coupling susbtrates. Instead, among the organic molecules, porphyrins and phthalocyanines, quite known as versatile species, offer the possibility to have a metallic core, facilitating any magnetic coupling. We consider the spinterface problem of the Fe-phthalocyanine over three prototypical transition-metal oxides substrates: CoO(001), NiO(001) and Cr_2O_3(0001).

The Density Functional Theory (DFT) approach has been used in the study of the electronic and magnetic ground-state properties. Hubbard corrections have been added to correct the Self-Screening Error of the substrates and of the molecule metallic centers. Van der Waals corrections as well have been added through specific exchange-correlation functionals to properly describe the long-range electrostatic interaction between the molecule and the substrate. The independent particle approximation (IPA) approach has been used instead in the study of the excitation properties. More demanding computations as GW + Bethe-Salpeter equation (BSE) calculations have been considered for the Fe-phthalocyanine in the isolated phase.

In the case of the Fe-phthalocyanine/NiO(001) spinterface a mapping between the DFT results and an Heisenberg model have been considered in order to understand the effect of the adsorption on the magnonic properties of the substrate.

Main results

(i) Over CoO(001) the Fe-phthalocyanine bonds through the O surface atoms to the Co underneath in an anti-ferromagnetic super-exchange fashion. The adsorbed system (molecule+substrate) optical transitions resemble the isolated molecule ones. A partial hybridization of the HOMO states of the molecule with the valence band of the substrate and the fact that the LUMO states of the molecule are inside the valence-conduction gap of the substrate suggest a light excitation can produce a charge transfer from the substrate to the molecule. Among other things, from the magnetic perspective the substrate during the adsorption shows simultaneously localized magnetism and itinerant magnetism behavior, making the spinterface particularly sensitive to external perturbations.

(ii) For what concern Cr_2O_3(0001), a first understanding of the substrate termination has been needed. Two main UHV terminations have been considered. Through an adiabatic approach the two terminations have been related. One characterized by protruding Cr atoms, antiferromagnetic, that we will call Cr-terminated, and the other one characterized by superficial O atoms, ferromagnetic at the surface and anti-ferromagnetic inside, that we will call O-terminated.

(a) Over Cr_2O_3(0001) in the Cr-terminated surface, the molecule binds through its imide N atoms to the surface, via a bidentate configuration, while the Fe atom acquires a ferromagnetic ordering with respect to the top Cr atoms, due to its proximity. The magnetic coupling is mainly localized at the interface.

(b) Over Cr_2O_3(0001) in the O-terminated surface, the molecule disposes its molecular axis along the crystalline axis of the substrate. Despite the weak binding, the effects on the substrate magnetic properties due to the adsorption are quite significant and propagate deeply inside the substrate. These studies are part of a collaboration with the experimental partners at Politecnico di Milano (POLIMI).

(iii) Over NiO(001) the Fe-phtahlocyanine bonds through the O surface atom to the Ni underneath as in the CoO(001); however, the super-exchange coupling is in this case much stronger. This spinterface does show mainly a localized magnetism behavior. From a magnonic perspective, the magnetic couplings at the interface are slightly modified by the adsorption, with consequent weak effects on the magnonic band structure. These studies are part of a collaboration with the theoretical partners at Institute of Molecular Science (ICMol) of Valencia.

(iv) A detailed analysis of the isolated molecule has been needed before these spinterfaces studies. In particular, it has emerged how the molecule is affected by Jahn-Teller distorsion in its ground-state configuration.

(v) During the study of these spinterfaces, the development of codes for the analysis of the results have been conducted. Moreover, a code has been developed for the calculation of the magnonic spectrum from an Heisenberg Hamiltonian, and of the BSE spectrum from a tight-binding Hamiltonian.

Organizational note

The present thesis consists of five parts, for a total of nine chapters. Part I is an introduction to organic spinterfaces, and to the theoretical and computational methods

used in the thesis to study them. Part II is an analysis of the Fe-phthalocyanine molecule ground-states and excited states. Part III is the study of the Fe-phthalocyanine/CoO(001) spinterface. Part IV is composed of three chapters: the first one is the analysis of the termination problem of the Cr_2O_3(0001) substrate, the second one and third is the study of the Fe-phthalocyanine/Cr_2O_3(0001) spinterfaces for the two plausible UHV terminations. Part V is composed of two chapters: the first one is the analysis of the Fe-phthalocyanine/NiO(001) spinterface from an electronic, magnetic and optical perspective, while the second one from a magnonic perspective.

Part I
Introduction

CHAPTER 1

The Spinterface Problem

While traditional electronics studies and exploits the interaction and dynamics of electrons as charged particles in a solid-state environment, spintronics (or spin electronics) takes into account their spin degrees of freedom, too, in the perspective of novel applications in information processing and storage [1]. In this regard, the main focus is on the mechanisms of spin injection/accumulation, spin transport, spin relaxation/de-phasing and spin detection. The presence of an interface can drastically modify these mechanisms, and an understanding of the electrons and their spin degrees of freedom in the proximity of the interface becomes necessary to explain these modifications.

1.1 Magnetoresistance effect

Let us consider the prototypical example of a spintronics phenomena: the magnetoresistance (MR) effect. Taken a magnetic/non-magnetic multi-layer system, the magnetization of the ferromagnetic layers can be manipulated through an external magnetic field. The change of the charge current resistance of the multi-layer system with respect to the relative magnetization of the ferromagnetic layers, is called the magnetoresistance effect. The microscopic origin of the effect depends on the nature of the non-magnetic layers. When the non-magnetic layers are insulating (spin conservation), the magneto-resistance effect is related to tunneling processes, and is thus called tunnel magneto-resistance effect (TMR) [14–16]. When the non-magnetic layers are metallic, the magneto-resistance effect is related to scattering processes, and is thus called giant magneto-resistance effect (GMR) [17, 18]. In both cases the resistance is related to the number of charge carriers in the two spin channels of the proximal magnetic layers. However, while in the tunneling process the phenomena is a spin-filtering one, in the scattering process there is an effective spin accumulation.

1.2 Spin relaxation and dephasing

The two phenomena above are examples of current spin injection/accumulation and transport mechanisms. The difference in the microscopic mechanisms translates in a difference in the characteristic parameters as the critical length scale: the tunneling length and the electron mean-free path, respectively. However, in addition to the electron mean-free path, in the case of spin transport phenomena, it is necessary to introduce two additional characteristic length scales: the spin relaxation and de-phasing lengths. These are related to processes of loss of spin accumulation or spin coherence in an ensemble of conductive electrons, due to the coupling of the conductive electron spin with the environment electric field (in a Zeeman-like way, considering a Lorentz transformation in

its local frame). The spin relaxation and de-pahsing mechanisms are then based on the spin-orbit interaction or on the hyperfine interaction. While the latter involves mainly strongly localized carriers at low magnetic fields, the former involves de-localized carriers and localized ones in the case of anisotropic exchange interactions as well as g-factor inhomogeneities [19]. Between the spin-orbit interaction ones, the D'yakonov-Perel' (DP - spatial inversion symmetry is broken) and the Elliott-Yafet (YE - spatial inversion symmetry is preserved) mechanism [20], are related not only to the spin-orbit interaction strength, but also to the momentum relaxation time [21]. Despite the spin-orbit interaction can be a problem in terms of spin coherence in transport properties, it is quite relevant in terms of spin detection and injection mechanisms. In fact, circularly polarized light can be used to produce (optical spin orientation) and detect (through selection rules) a spin polarized excited state [22–25].

An example of the relevance of spin-orbit coupling in optical orientation is clearly underlined in [1] for the case of GaAs. If we indicate by n_+ and n_- the density of electrons polarized parallel and antiparallel to the light propagation direction, we can define the spin polarization of an electronic state as

$$P = (n_+ - n_-)/(n_+ + n_-) \tag{1.1}$$

The helicity of the exciting light is indicated by $\sigma^{\pm}$, and the corresponding dipole is used to evaluate the probabilities of the different optical excitations, which are reported in Fig. 1.1 panel (b). If the photon energy is between E_g and $E_g + \Delta_{so}$, then

$$P = (1 - 3)/(1 + 3) = -1/2 \tag{1.2}$$

the electronic state is spin polarized, in the direction against the one of the light propagation. If instead the photon energy is greater than $E_g + \Delta_{so}$, then the excited electronic state is not anymore spin polarized. Therefore, the spin-orbit interaction, through the splitting of the electronic bands in Γ (i.e. Γ_8 and Γ_7), allows us to produce spin polarized populations through light excitation.

Naively, the spin-orbit interaction offers a channel between the local electric field due to the nuclei and the spin degrees of freedom of the electrons: so it represents a possible dissipative (source) channel in the case of spin relaxation and de-phasing mechanisms or a possible source (dissipative) channel in the case of optical orientation.

1.3 Organic spintronics and spinterfaces

With the aim to partially reduce the transport spin relaxation and dephasing mechanisms, organic materials have been added to the spintronic devices, initiating the field of organic spintronics [26]. This addition has however led to new difficulties. Among them, a relevant one is the necessity to use current spin injection mechanisms instead of optical ones, and the consequent conductivity mismatch, due to the low carrier mobility of the organic materials (being the hopping the main transport mechanism) [27]. This translates in a strong dependence of the transport properties on the interfacial spin polarization. An example is the local inversion of the giant magnetoresistance effect after the substitution of the metallic layer with an organic semi-conductive one [2] (these phenomena are not observed at inorganic-inorganic compounds interfaces).

The interface spin properties appear to be so relevant for explaining the observed phenomena in organic-inorganic materials that the term *spinterface* has been coined to indicate them [28, 29]. Due to the lack of accurate microscopic characterizations, the

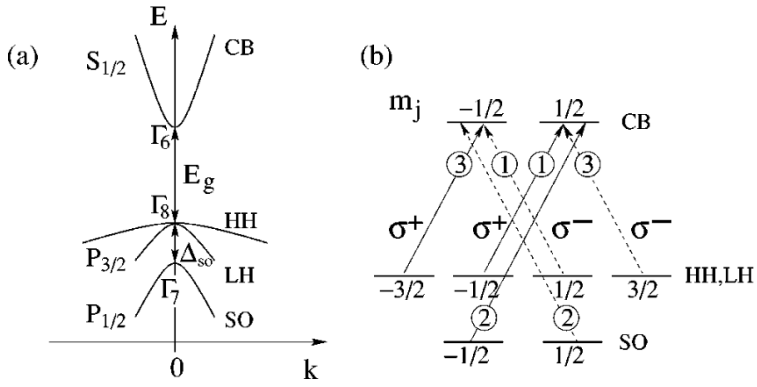

Figure 1.1 Interband transitions in GaAs: (a) schematic band structure of GaAs near the center of the Brillouin zone (Γ point), where E_g is the band gap and Δ_{so} the spin-orbit splitting; CB, conduction band; HH, valence heavy hole; LH, light hole; SO, spin-orbit split-off subbands; $\Gamma_{6,7,8}$ are the corresponding symmetries at the $k = 0$ point, or, more precisely, the irreducible representations of the tetrahedron group T_d (Ivchenko and Pikus, 1997); (b) selection rules for interband transitions between the m_j sublevels for circularly polarized light σ^+ and σ^- (positive and negative helicity). The circled numbers denote the relative transition intensities that apply for both excitations (depicted by the arrows) and radiative recombinations. Reproduced from [1].

spinterface states are often studied in single molecule systems, due to their intrinsic locality; so that organic spintronics is understood in terms of the simpler, but still significantly complex, molecular spintronics [30]. In this regard, the explanation of the local inversion of the giant magnetoresistance effect mentioned above, assumes a very simple form as we now discuss.

Let us consider the adsorption of an arbitrary organic molecule on a magnetic metallic substrate, and let us take a look at the density of states (DOS) projected on the two: molecule and substrate. The proximity of the substrate shifts and spreads the molecular levels, due to hybridization mechanisms. Let us focus at this point on two possible cases in which the molecule acts as a spin filter, the ones reported in Fig. 1.2 panels (b) and (c). In the second case the molecule increases the number of carriers in the majority spin channel, while in the first case the molecule reverse the majority spin channel.

Despite the fact that in the above example no modifications are depicted in the substrate, generally speaking spinterface states are the result of coordination chemistry and electronic band structure modifications [31, 32]. A proper understanding of the spinterface states, in fact, requires a simultaneous study of the molecular and substrate components. This shift of the energy states, which differ in the two spin channels, is due to the Stoner exchange.

From the molecular perspective, in molecular electronics a distinction between two adsorption regimes is usually considered: weak coupling (physisorption) and strong coupling (chemisorption) [33–35]. In the former no strong chemical bonds are built, and the molecule largely retains its gas phase electronic structure; in the latter the molecule electronic structure is significantly perturbed, as a consequence of the formation of chemical bonds. It is important to note that this is a simplification; in reality, many molecular systems involving organic molecules on metallic substrates exhibit an intermediate cou-

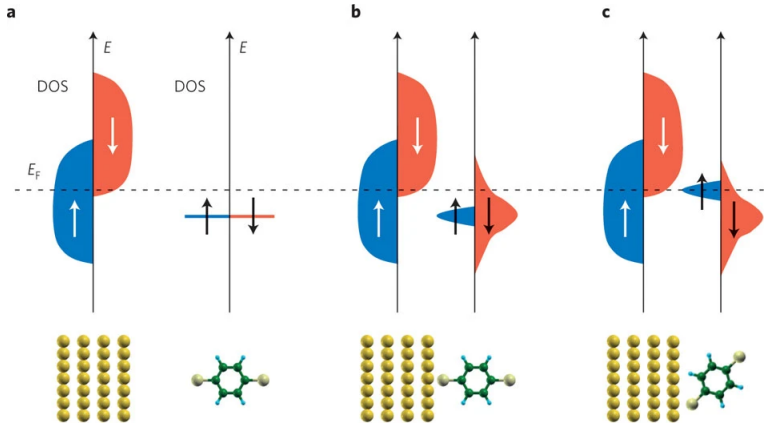

Figure 1.2 (a), When the magnetic metal (left) and the molecule (right) are well separated, the overall density-of-states (DOS) is simply the superposition of the individual DOS of the two spin components (blue represents the spin-up DOS and red the spin-down DOS) — that is, a broad spin-polarized DOS for the metal and a series of discrete energy levels for the molecule. In this case, the DOS of the metal alone determines the spin-polarization of the tunnelling current. b,c, When the molecule is brought into contact with the metal the DOS gets modified into two ways: the energy levels broaden (b) (the broadening is exaggerated in the figure) and their position shifts in energy (c). In both cases new peaks in the DOS might appear at the EF of the electrodes, arising from new hybrid interfacial states. It is this new DOS that determines the spin-polarization of the injected current, which can be dramatically different, and even reversed, compared with the polarization of the electrodes (as in (b)). Reproduced from [2].

pling regime [36]. In the case of spinterface states, we expect not only a chemical bonding, but also a spin-dependent broadening and shift of the energy levels (spin dependent chemisorption), as already naively observed above.

Analogously, from the substrate perspective, we can expect both, slight spin related variations and more significant ones: an increase in the magnetic anisotropy [37], a magnetic hardening [3], or in the case of hetero-structures a variation in the intra-layer magnetic coupling [38, 39]. In this regard, in Fig. 1.3 we report the measures [3] of the magnetic hardening in thick Co films (7 nm) due to the adsorption of C_{60} and Gaq_3.

Through a radiofrequency (rf) field the electronic magnetic moments are excited, due to their coupling to the nuclear spins (hyperfine coupling). The optimal rf field is the one giving maximum spin-echo signal from the sample (maximum magnetic response), and is related to the electronic magnetic susceptibility. An increase in the optimal rf field witnesses an increase in magnetic hardening, as reported in Fig. 1.3 (a) (the ratio with the sample value eliminates possible spurious contributions). The partial flatness of the ratio assures that the films (molecules-substrate) are homogeneous on a mesoscopic scale. The hysteresis loops in Fig. 1.3 (b), extracted from measurements of the longitudinal magneto-optic Kerr effect (L-MOKE), confirm the enhancement of the coercive fields.

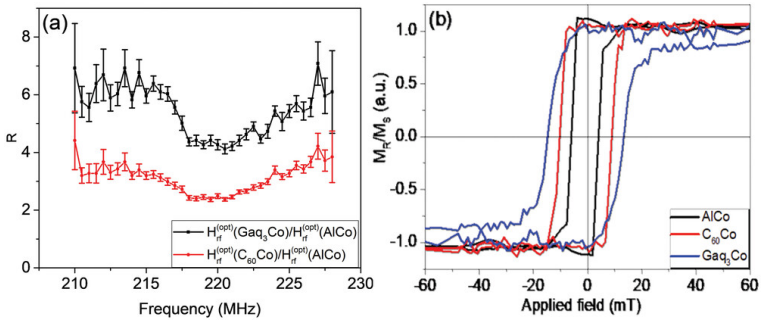

Figure 1.3 a) Ratio R of the optimal rf field of the Co/molecule systems ($H_{rf}^{(opt)}(X)$) divided by the optimal rf field of the reference sample ($H_{rf}^{(opt)}(Al)$), proportional to the ratio between the mean enhancement factor of the Co/molecule system and the corresponding of the reference sample. b) L-MOKE normalized hysteresis loops at 77 K for Gaq_3-Co and C_{60}-Co. The applied field direction is the same as the rf field in NMR experiments. Reproduced from [3].

1.4 Phthalocyanines and porphyrines in spinterfaces

Among the different organic molecules used in these studies, the preferential ones are the organo-metallic ones, e.g. metal-phthalocyanines and metal-porphyrines [40–42], where a central magnetic core, a transition-metal or lanthanide atom, is bonded to an external organic macro-cycle [43–46]. The magnetic core, in fact, can facilitate the coupling of the molecule with the substrate [47]. Thus, these molecules have great application potential, beyond spintronic devices [48–50], as photosensitizers [51], electrocatalysts for CO_2 or O reduction [52–55], bifunctional catalysis for lithium-oxygen batteries [56, 57], and energy haversting from singlet fission [58].

There are a few studies of metal-phtalocyanines on metallic surfaces, as copper [59], gold [60], silver [61] and nickel [62], and Co [63], passivated by a graphene layer to partially decouple the molecule and the substrate, and directly on graphene [64]. In these studies, focus is given to the dependence of the adsorption properties, as the molecule-substrate coupling and hybridization of the orbitals, on the metallic ion centre. In fact, as reported in the study of the Fe-phthalocyanine and Cu-phthalocyanine on a graphene/Co substrate [4], a different magnetic molecular core (Fig. 1.4) translates into a different magnetic molecule-substrate coupling. Both X-ray magnetic circular dichroism (XMCD) measurements and DFT calculations confirm a parallel magnetization between the Co substrate and the magnetic molecular core in the case of Fe, while an opposite one in the case of Cu. When a metallic substrate is considered, the need of O-passivation or of an intermediate insulating layer is required in case of strong molecule-substrate coupling, to partially preserve the molecular nature.

Thus, despite organic compounds were initially studied in terms of transport properties, when interfaced with inorganic compounds they showed new unexpected phenomena. This has brought to question the subtle bonding mechanisms at these interfaces, and the interest into understanding their magnetic properties. From here the origin of the word *spinterfaces* and the significant research about them.

Hence, analogue studies have been conducted for metal-(tetraphenyl) porphyrines on O-passivated iron [65], O-passivated ultrathin Ni, and Co magnetic films on Cu(001)

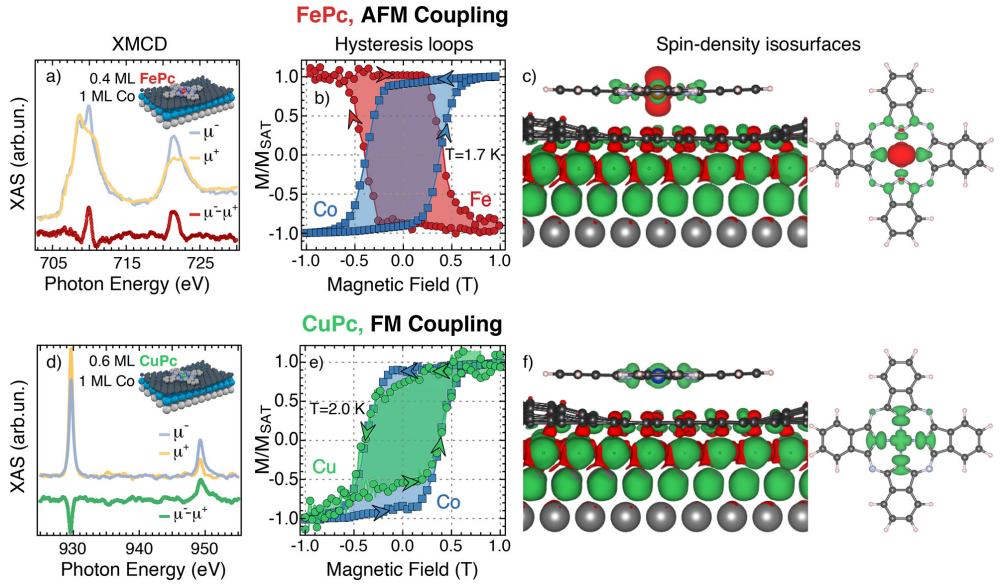

Figure 1.4 XMCD from Fe and Cu $L_{2,3}$ absorption edges (a,d), element-resolved hysteresis loops of FePc (b) and CuPc (e) on Gr/1 ML Co. The change in the sign of the XMCD (a,d) and of the field-dependent magnetization (b,e) indicates an AFM alignment for FePc/Gr/Co and a FM one for CuPc/Gr/Co. Spin-density isosurfaces plots for FePc and CuPc on Gr/Co/Ir (side and top view with hidden substrate), computed at the DFT-PBE+U level, U = 4 eV (c,f). The geometry optimization included PBE-D2 van der Waals corrections. Green (red) isosurfaces correspond to the up (down) spin density. Reproduced from [4].

substrates [66].

1.5 Magnon spintronics

The O passivization to avoid the disaggregation of the molecule during the adsorption originates the idea to consider directly oxides as susbstrates, due to their insulating character. In these regard, there are as well a few studies on metal-phthalocyanines, e.g. adsorbed on In_2O_3 [67], on SrTiO [68], on TiO_x and on MoO_x [69, 70], on CoO [71] and on MnO [72]. Analogue studies have been done for metal-porphyrines, as the ones on TiO_2 and SnO_2 [73, 74]. However, from a spintronic transport perspective, the loss of a conductive character means that now the substrate can not anymore sustain spin currents of electrons.

However, in a magnetic material, information can be also carried by coherent collective magnetic excitations, i.e., spin waves (SW), and not only electrons, as extensively studied in the field of magnon spintronics [75]. While from a classical point of view spin waves represent phase coherent precessions of local magnetic moments, from a quantum point of view their quanta, called magnons, behave as weakly interacting bosonic quasi-particles [76, 77]. The effects on the spin waves properties of insulating magnetic substrates due to the formation of a spinterface have already been studied [78, 79], and observed. In [5] spin waves are generated electrically through spin Hall effect [80] and

thermally through spin Seebeck effect [81], these then propagate inside a $Y_3Fe_5O_{12}$ substrate. The measure of the voltage difference between the injector and the detector at different distances (Fig. 1.5 panels (a) and (b)), allows to extract the magnon diffusion length, which increases after the adsorption of a CoPc molecule layer (Fig. 1.5 panel (c)).

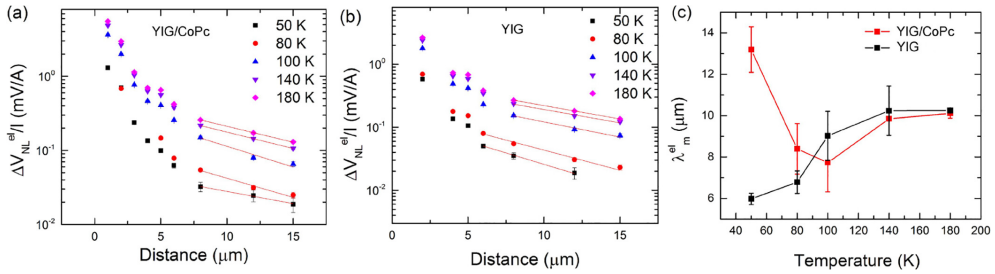

Figure 1.5 Nonlocal voltage amplitude normalized to the applied current as a function of injector–detector distance for the electrically generated magnon current in devices with (a) or without (b) a CoPc overlayer. The red lines are the linear fit in the exponential region from which the magnon diffusion length is extracted. All measurements were performed with an applied current of 100 μA and an external magnetic field of 300 Oe. (c) Magnon diffusion length as a function of temperature for the electrically generated magnon current in devices with and without a CoPc overlayer. Reproduced from [5].

1.6 Spinterface activation

Through light the spinterface states could be manipulated, and the magnetic properties of the substrate actively tuned. The activation/manipulation of the spinterface/interface states is a problem subject to extensive research [82]: not only through light excitation [83], but also via functionalization [84, 85] and adsorption site selection [86, 87]. The nickel tetraphenyl porphyrin spin moment, acquired after adsorbing on Cu(100), can be reversibly manipulated through a nitrogen dioxide ligation (Fig. 1.6) [6].

In our research, we focused on spinterfaces on antiferromagnetic materials. The spinterface is used as a light channel to produce/tune/detect THz coherent magnetic excitations in the antiferromagnetic material, which would be otherwise insensitive to any external optical perturbation [88–92].

There are different plausible mechanisms for the organic/inorganic spinterface light activation of magnons: one is the mechanical deformation of the interface due to the light excitation of the molecule [93], with consequent straintronics [7] effects on the substrate, another one is the charge movement at the interface in a spin-unbalanced way [94]. The two paths are fundamentally related to the dynamical mechanisms of magnon-phonon coupling [95] and magnon-exciton coupling [96]. In both cases, a significant ingredient for the coupling is the spin symmetry breaking; in fact we can not expect to excite magnons without producing a spin unbalance. In Fig. 1.7 the magnon dispersion of a CrSBr monolayer, after uniaxial strain is applied along the primitive axis of the unit cell.

The differences in the involved time-scales of the two above light activation mechanisms (in the former mechanism a nuclei motion is expected), and the fact that the effect of the deformation on the magnetic couplings is not as significant as the charge-movement one [79], make us focus on the latter in the perspective of spinterface light activation.

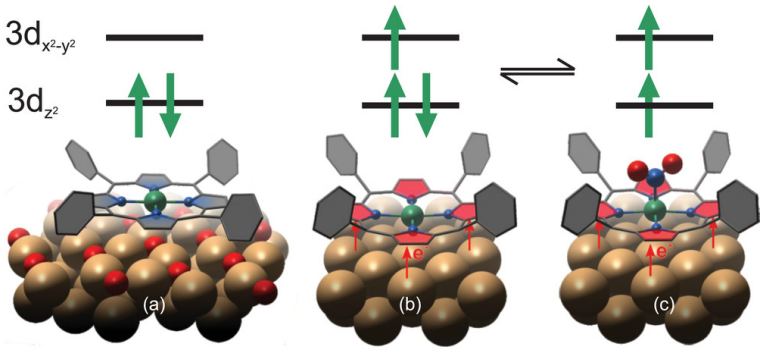

Figure 1.6 Schematic representation of the behavior of the NiTPP/Cu(100) interface. The magnetic properties are dominated by the central Ni ion (green), while the frontier orbitals that determine the transport, as well as the optical properties, are localized on the macrocycle moiety (depicted in red). In a free NiTPP molecule, the Ni ion is in the [Ni(II), S = 0] state. a) The situation is well reproduced when NiTPP is deposited on an oxygen-reconstructed Cu(100) surface (oxygen atoms in red). b) If NiTPP is in direct contact with the Cu(100) surface, interface charge transfer leads to a reduction of the Ni ion to a [Ni(I), S = 1] state. c) Exposure to NO2 induces a transition to a new [Ni(II), S = 1] state. Although the spin state of NiTPP changes between (b) and (c), the frontier orbitals remain unchanged. They are stabilized by the strong interface charge transfer into the macrocycle moiety. Reproduced from [6].

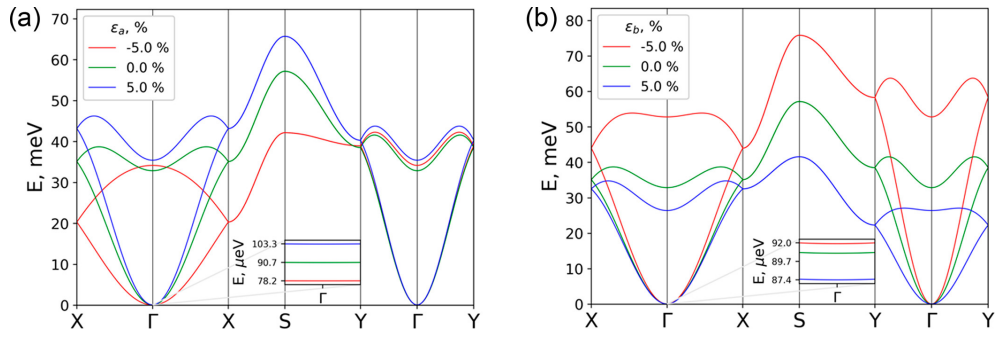

Figure 1.7 Magnon dispersion of the CrSBr monolayer (U = 3 eV): (a) uniaxial strain in the a axis and (b) uniaxial strain in the b axis. Inset: anisotropic gap at the Γ point. Reproduced from [7].

1.7 The SINFONIA project

This thesis work is founded within the efforts of a European Union's Horizon 2020 Research and Innovation program under grant agreement no. 964396 FET-Open SINFONIA (Selectively activated INFormation technology by hybrid OrgaNIc interfAces). The main objective of the project is to exploit the hybridized states at the interface between an antiferromagnet, decoupled from any external electromagnetic perturbation, and a molecular system, in the perspective of producing/detecting magnetic perturbations, of the spin-excitation kind due to the insulating character of the chosen antiferromagnets, through an optical stimulus.

The consortium consists of different partners: Politecnico di Milano (POLIMI) with the role of preparation and characterization of the hybrid organic/antiferromagnetic interfaces, Universita' degli Studi di Milano (UMIL) with the role of theoretical development of hybrid organic/antiferromagnetic interfaces, Technische Universitat Dortmund (TUDO) with the role of optical control of these hybrid organic/antiferromagnetic nanosystems, Asociacion Centro de Investigacion Cooperativa en Nanociencias CIC nanoGUNE (CIC nanoGUNE) with the role of propagation of spin-waves through these low-dimensional hybrid systems, and Consiglio Nazionale delle Ricerche (CNR) with the role of communication, dissemination and exploitation activities. Between the partners we collaborated with the experimental counterpart at POLIMI trying to help them understanding the results of Cr_2O_3 through our theoretical effort, and with the theoretical counterpart at Instituto de Ciencia Molecular (ICMol) referring to the CIC nanoGUNE, using different ways than the usual approaches to study the chemical tuning of the substrates magnetic properties.

In the SINFONIA project contest this thesis is dedicated to the theoretical study of some prototypical spinterfaces: the ones formed by the adsorption of a metal-organic molecule (Fe-phthalocyanine), which is largely studied in the contest of spintronics, on the three prototypical transition-metal oxides CoO, NiO and Cr2O3, with high Neel temperature and insulating character, in order to favour antiferromagnetic character and spin-excitation transport.

CHAPTER 2

Density functional theory and beyond

In this chapter we introduce the theoretical and computational methods used in this thesis. The many-body theory of the electronic problem is simplified through the use of effective theories, as density functional theory and Green's function approaches. The main quantity of the system is not anymore the full many-body wave-function, but the electronic charge density or the electron propagator. The corresponding computational methods are introduced, and the details due to the specific studied spinterfaces highlighted.

2.1 The many-electron problem

A quantum mechanical system of N particles is described through the wave-function $|\Psi\rangle$, which depends on the particle position and spin-degrees of freedom. The static ground-state and excited-state wave-functions are eigenstates of the Hamiltonian operator of the N particles system

$$\hat{H}\,|\Psi\rangle = E\,|\Psi\rangle \tag{2.1}$$

In case of time-dependent problems the evolution of the system is instead solved considering the equation

$$i\hbar\frac{d}{dt}\,|\Psi\rangle = \hat{H}\,|\Psi\rangle \tag{2.2}$$

The Hamiltonian operator for a system of interacting electrons in an external potential such as that generated by the interaction with positive charges (nuclei) has the following form

$$\hat{H} = \hat{T} + \hat{W} + \hat{U} \tag{2.3}$$

$$\hat{T} = -\sum_i \frac{\hbar^2 \boldsymbol{\nabla}_{\boldsymbol{i}}^2}{2m} \tag{2.4}$$

$$\hat{W} = \frac{e^2}{8\pi\epsilon_0}\sum_{ij}\frac{1}{|\boldsymbol{r}_i - \boldsymbol{r}_j|} \tag{2.5}$$

$$\hat{U} = \sum_i u(\boldsymbol{r}_i) \tag{2.6}$$

with a kinetic contribution $\hat{T}$, an interaction contribution between pair of particles at positions in space $\boldsymbol{r}_i$, and an external contribution $\hat{U}$ (where ϵ_0 is the vacuum permittivity) .

Due to the numerous degrees of freedom of the wave-function, the problems 2.1-2.2 are numerically demanding, and most of the time the interest is not into finding the full many-body wave-function. In fact, the majority of the information of the wave-function is integrated out, when observables are considered. So instead of considering the entire wave-function and solve the N particles system in its entirety, effective theories which consider only a few of the numerous degrees of freedom are employed. Between the most used approaches are the (time-dependent) Density Functional Theory (DFT) approach, in which the N particles system density is considered instead

$$n_\sigma(\boldsymbol{r}t) = \sum_{\sigma_2,\dots\sigma_N} \int \cdots \int d\boldsymbol{r}_2 \dots d\boldsymbol{r}_N |\Psi(\boldsymbol{r}\sigma, \boldsymbol{r}_2\sigma_2, \dots, \boldsymbol{r}_N\sigma_N, t)|^2 \tag{2.7}$$

or the Reduced Density Matrix approach, in which the correlation between a number of space points, at two different times is considered (in the case of 1-particle reduced density matrix)

$$\rho(\boldsymbol{r}\sigma t, \boldsymbol{r'}\sigma' t') = \sum_{\sigma_2,\dots\sigma_N} \int \cdots \int d\boldsymbol{r}_2 \dots d\boldsymbol{r}_N \Psi(\boldsymbol{r}\sigma, \boldsymbol{r}_2\sigma_2, \dots, \boldsymbol{r}_N\sigma_N, t)^* \tag{2.8}$$

$$\times \Psi(\boldsymbol{r'}\sigma', \boldsymbol{r}_2\sigma_2, \dots, \boldsymbol{r}_N\sigma_N, t') \tag{2.9}$$

If a Quantum Field Theory (QFT) approach is considered, other effective theories can be found. In QFT the particles are excitation quanta of an abstract quantity called field $\hat{\psi}(\boldsymbol{r}\sigma t)$. So instead of solving the N particles system, the field problem is considered, and the number of particles is not anymore fixed. The field problem reduces into solving the Heisenberg equation of the field operator

$$i\hbar \frac{d}{dt}\hat{\psi}(\boldsymbol{r}\sigma t) = [\hat{H}, \hat{\psi}(\boldsymbol{r}, \sigma, t)] \tag{2.10}$$

where $[\cdot,\cdot]$ is the commutator operator and the Hamiltonian has now the following form

$$\hat{H} = \hat{T} + \hat{W} + \hat{U} \tag{2.11}$$

$$\hat{T} = -\int d\boldsymbol{r}\hat{\psi}^\dagger(\boldsymbol{r}\sigma t)\frac{\hbar^2\boldsymbol{\nabla}^2}{2m}\hat{\psi}(\boldsymbol{r}\sigma t) \tag{2.12}$$

$$\hat{W} = \frac{e^2}{8\pi\epsilon_0}\sum_\sigma \int\int d\boldsymbol{r}d\boldsymbol{r'}\frac{1}{|\boldsymbol{r}-\boldsymbol{r'}|}\hat{\psi}^\dagger(\boldsymbol{r}\sigma t)\hat{\psi}^\dagger(\boldsymbol{r'}\sigma t)\hat{\psi}(\boldsymbol{r'}\sigma t)\hat{\psi}(\boldsymbol{r}\sigma t) \tag{2.13}$$

$$\hat{U} = \sum_\sigma \int d\boldsymbol{r}u(\boldsymbol{r}\sigma t)\hat{\psi}^\dagger(\boldsymbol{r}\sigma t)\hat{\psi}(\boldsymbol{r}\sigma t) \tag{2.14}$$

An additional constraint has to be considered in the solution of the field operator problem: the field operator has to satisfy the following commutation relations as well

$$[\hat{\psi}^\dagger(\boldsymbol{r}\sigma t), \hat{\psi}(\boldsymbol{r'}\sigma' t')]_\pm = \delta_{\sigma\sigma'}\delta(t-t')\delta(\boldsymbol{r}-\boldsymbol{r'}) \tag{2.15}$$

where $+$ points to fermionic systems and $[\cdot,\cdot]_+$ is the anti-commutator operator, while $-$ points to bosonic systems and $[\cdot,\cdot]_-$ is the usual commutator operator (this is related to the anti-symmetrization/symmetrization of the N particles system wave-function). Given a state of the system $|\Psi\rangle$, a particle is then described as a quantum excitation of the field operator over the state of the system

$$\psi(\boldsymbol{r}\sigma t) = \hat{\psi}(\boldsymbol{r}\sigma t)^\dagger |\Psi\rangle \tag{2.16}$$

Note that in QFT the state of the system is usually expressed through the density matrix, which at equilibrium assumes the following form

$$\hat{\rho} = \frac{e^{-\beta \hat{H}}}{\mathrm{Tr}\{e^{-\beta \hat{H}}\}} \tag{2.17}$$

where $\beta = 1/k_B T$ with k_B the Boltzmann's constant and T the temperature of the system. Projected over the eigenstates Ψ_n of the many particles system, the density matrix above assumes the form

$$|\Psi\rangle = \sum_n e^{-\beta \hat{E}_n} |\Psi_n\rangle \tag{2.18}$$

In case of zero temperature $\beta \to \infty$ the state of the system is exactly the ground-state of the system $|\Psi_0\rangle$.

In non-relativistic QFT, in the case of a fermionic system, the ground-state is represented by the Fermi sea, defined by the filling of the electrons of the lowest energy states. In this case the annihilation of an excitation quantum corresponds to the creation of a hole in the Fermi sea

$$\hat{\psi}(\boldsymbol{r}\sigma t)\,|\Psi_0\rangle \neq 0 \tag{2.19}$$

This QFT formalism is the foundation of the Green's function approach introduced in Section 2.3. In fact, instead of considering the above field operator problem, it is common to consider the associated Green's function problem and to treat the interaction $\hat{W}$ perturbatively. The M-bodies Green's function is related to the amplitude of the process of propagation of M excitation quanta over the state of the system (1-body Green's function)

$$G(\boldsymbol{r}\sigma t, \boldsymbol{r'}\sigma' t') = \langle \Psi | T\{\hat{\psi}(\boldsymbol{r}\sigma t)^\dagger \hat{\psi}(\boldsymbol{r'}\sigma' t')\} | \Psi \rangle \tag{2.20}$$

where $T\{\}$ is the time-ordering operator.

2.2 Density functional approach

The Hohenberg-Kohn theorem [97] assures us that any observable of a N particles system can be expressed as a functional of the ground-state density, and that the energy of the system as a functional of the density is minimal when the density is the ground-state density

$$E[n] = T[n] + W[n] + U[n] \tag{2.21}$$

Unfortunately, we do not know the functional dependence of the energy. In this regard, however, the Kohn-Sham assumption [98], which states that the interacting problem density is equal to the density of a fictitious non-interacting problem, allows us to partially express this functional dependence

$$E_{KS}[n] = T_{KS} + E_{Hxc}[n] + U[n] \tag{2.22}$$

where the kinetic term is the one of a non-interacting problem, while the interaction has been factorized into an electrostatic term E_H and a exchange-correlation term E_{xc}

$$E_{Hxc}[n] = E_H[n] + E_{xc}[n] = \sum_\sigma \int\int d\boldsymbol{r}\boldsymbol{r'} \frac{n(\boldsymbol{r}\sigma) n(\boldsymbol{r'}\sigma')}{|\boldsymbol{r} - \boldsymbol{r'}|} + E_{xc}[n] \tag{2.23}$$

The fictitious particles, whose density is the real ground state one, solve the mean-field problem

$$-\frac{\hbar^2\boldsymbol{\nabla}^2}{2m}\psi_i(\boldsymbol{r}\sigma)+\frac{e^2}{8\pi\epsilon_0}\int d\boldsymbol{r'}\frac{n(\boldsymbol{r'}\sigma)}{|\boldsymbol{r}-\boldsymbol{r'}|}\psi_i(\boldsymbol{r}\sigma)+V_{xc}[n]\psi_i(\boldsymbol{r}\sigma)=\epsilon_i\psi_i(\boldsymbol{r}\sigma) \tag{2.24}$$

where the second and third terms (Hartree and exchange-correlation, respectively) form the Kohn-Sham potetnial.

The fact that the problem of the functional dependence of the energy of the system has been reduced to the problem of the functional dependence of a mean-field potential of fictitious free-particles, in reality is a step forward in terms of solving of the problem. Indeed, we can guess a plausible form for the Kohn-Sham potential (exchange-correlation part). In this guess, the accuracy of the solution of the density functional theory (DFT) problem resides [99].

In the case of time-dependent problems analogue quantities and properties can be obtained from a route similar to the DFT one, called time-dependent DFT (TDDFT) with analogue theorems and approximations as the DFT [100, 101].

2.3 Green's function approach

The introduction of Green's functions in the QFT approach and of the interaction between particles perturbatively, allow us to map the N particles problem into a closed system of integro-differential equations, called the Hedin's equations [102, 103]

$$G(12)=G_0(12)+\int d'1d'2G_0(11')\Sigma(1'2')G(2'2) \tag{2.25}$$

$$W(12)=v(12)+\int d1'd2'v(11')\Pi(1'2')W(2'2) \tag{2.26}$$

$$\Sigma(12)=i\int d3d4\Gamma(413)G(32)W(42) \tag{2.27}$$

$$\Pi(12)=-i\int d3d4\Gamma(134)G(23)G(42) \tag{2.28}$$

$$\Gamma(123)=\delta(12)\delta(13)+\int d4d5d6d7\Gamma(145)G(64)G(57)\frac{\delta\Sigma(23)}{\delta G(67)} \tag{2.29}$$

where the notation $1=\boldsymbol{r}_1\sigma_1t_1$ has been used, and where $v(12)=(e^2/8\pi\epsilon_0)(1/|\boldsymbol{r}_1-\boldsymbol{r}_2|)\delta(t_1-t_2)\delta_{\sigma_1\sigma_2}$ is the Coulomb potential, while G_0 is the Green's function of the interacting system at the Hartree order. The quantities above are respectively the self-energy Σ, the screened potential W, the polarizability Π and the interaction vertex Γ.

Differently from the DFT approach in this case we know all the functional dependences, but the cost is that the equations to solve are now more demanding in terms of computational effort. So as in DFT, also in this QFT approach some approximations are made, typically the GW one [104]:

$$\Gamma(123)=\delta(12)\delta(13) \tag{2.30}$$

from which follows the name of the approximation

$$\Sigma(12)=iG(12)W(12) \tag{2.31}$$

Usually, only one cycle of the Hedin's equations is considered in the GW approximation, i.e. $\Sigma = G_0W_0$, and the G_0 used is the Kohn-Sham one obtained from a previous DFT calculation [105]. The obtained $\Sigma_{G_0W_0}$ is then used to correct the Kohn-Sham energies

$$\epsilon_i = \epsilon_i^{KS} + \frac{Re\,\langle\psi_i^{KS}|\Sigma_{G_0W_0}(\omega) + V_x - V_{xc}|\psi_i^{KS}\rangle}{\langle\psi_i^{KS}|1 - d\Sigma_{G_0W_0}(\omega)/d\omega|\psi_i^{KS}\rangle}\Bigg|_{\omega=\epsilon_i^{KS}} \tag{2.32}$$

where V_{xc} is the Kohn-Sham exchange-correlation potential, V_x is the nonlocal Hartree-Fock exchange potential and ψ_i^{KS} is the Kohn-Sham state i-th associated to the Kohn-Shame energy ϵ_i^{KS}.

2.3.1 Two-particle properties

The QFT approach is mainly considered in the study of the excitated states of a N particles system [106]. The direct photoemission and inverse photoemission are, in fact, related to the immaginary part of the 1-body Green's function, while the absorption spectrum is related to the polarizability, which is equal to a contraction of the 2-body Green's function. The polarizability can be directly obtained from the Hedin's equations; however, to consider the two-body Green's function instead, and its Dyson-like equation, called Bethe-Salpeter equation (BSE), is much more convenient. In fact, this Bethe-Salpeter equation can be mapped into the solution of a two-particle Hamiltonian indicated as H^{2p}. The Bethe-Salpeter equation has the following form [107]

$$L(121'2') = L_0(121'2') + L_0(13'^+1'3^+)\Xi(3^+2^+3'^+2'^+)L(2'^+22^+2') \tag{2.33}$$

$$L(121'2') = -G_2(121'2') + G(11')G(22') \tag{2.34}$$

where $1^+ = \boldsymbol{r}\sigma t^+$ with $t^+ = \lim_{\epsilon\to 0}(t+\epsilon)$, and G_2 is the 2-body Green's function, while L_0 the interacting system solution at the Hartree order. The reduction into the two-particle Hamitlonian is obtained expressing the BSE in terms of the orthonormal orbitals n_i that diagonalize L_0

$$L^{n_4n_2}_{n_1n_3}(t+i\epsilon) = [L_0^{-1} + \frac{i}{2}\Xi]^{-1}{}^{n_4n_2}_{n_1n_3} = 2i[H^{2p} - I(t+i\epsilon)]^{n_4n_2}_{n_1n_3}(f_{n_2} - f_{n_4}) \tag{2.35}$$

Optical excitations involve transitions between occupied and empty states, so only these combinations of indices are needed in H^{2p}. We will indicate the transitions $t = (n_4) \to (n_2)$ as resonant transitions $r = (v\boldsymbol{k} - \boldsymbol{q}) \to (c\boldsymbol{k})$ and as anti-resonant transitions $a = (c\boldsymbol{k}) \to (v\boldsymbol{k} + \boldsymbol{q})$, where c indicates a conduction state while v a valence state, and $\boldsymbol{k}$ its corresponding crystal momentum. The two-particle Hamiltonian assumes then the following block form in the long-wavelength limit $\boldsymbol{q} \to 0$

$$H^{2p} = \begin{pmatrix} H_{rr} & H_{ra} \\ -(H_{ra})^* & -(H_{rr})^* \end{pmatrix} \tag{2.36}$$

Writing the two main elements of the Hamiltonian in terms of the generalized dipole elements

$$\rho_{\sigma(n1,\boldsymbol{k1})(n2,\boldsymbol{k2})}(\boldsymbol{G};\boldsymbol{p1},\boldsymbol{p2},\boldsymbol{q}) = \langle n1\boldsymbol{k1} - \boldsymbol{p1}|\, e^{i(\boldsymbol{q}+\boldsymbol{G})\cdot\hat{\boldsymbol{r}}}\,|n2\boldsymbol{k2} - \boldsymbol{p2}\rangle \tag{2.37}$$

we have for the resonant part $r = (\sigma_c c\sigma_v v\boldsymbol{k})$:

$$H_{rr'} \quad = \quad E_r\delta_{rr'} + (f_M v_{rr'} - W_{rr'}) \tag{2.38}$$

where

$$
\begin{aligned}
v_{rr'} &= \frac{1}{\Omega}\sum_{\boldsymbol{G}\neq\boldsymbol{0}} v(\boldsymbol{q}+\boldsymbol{G})(\rho_{\sigma_{c'}(c'\boldsymbol{k'})(v'\boldsymbol{k'}-\boldsymbol{q})}(\boldsymbol{G},\boldsymbol{q}))^{*}\rho_{\sigma_c(c\boldsymbol{k})(v\boldsymbol{k}-\boldsymbol{q})}(\boldsymbol{G},\boldsymbol{q})\delta_{\sigma_c\sigma_v}\delta_{\sigma_{c'}\sigma_{v'}} \\
W_{rr'} &= \frac{1}{\Omega}\sum_{\boldsymbol{G}\boldsymbol{G'}} W_{\boldsymbol{G}\boldsymbol{G'}}(\boldsymbol{k'}-\boldsymbol{k})(\rho_{\sigma_{c'}(c'\boldsymbol{k'})(c\boldsymbol{k})}(\boldsymbol{G},\boldsymbol{k'}-\boldsymbol{k}))^{*}\times \\
&\quad\times\rho_{\sigma_{v'}(v'\boldsymbol{k'}-\boldsymbol{q})(v\boldsymbol{k}-\boldsymbol{q})}(\boldsymbol{G'},\boldsymbol{k'}-\boldsymbol{k})\delta_{\sigma_{c'}\sigma_c}\delta_{\sigma_{v'}\sigma_v}
\end{aligned}
$$

while for the coupling part, considering $a=(\sigma_c c\sigma_v v\boldsymbol{k})$:

$$H_{ra'} = (f_M v_{ra'} - W_{ra'}) \tag{2.39}$$

where

$$
\begin{aligned}
v_{ra'} &= \frac{1}{\Omega}\sum_{\boldsymbol{G}\neq\boldsymbol{0}} v(\boldsymbol{q}+\boldsymbol{G})(\rho_{\sigma_{v'}(v'\boldsymbol{k'}+\boldsymbol{q})(c'\boldsymbol{k'})}(\boldsymbol{G},\boldsymbol{q}))^{*}\rho_{\sigma_c(c\boldsymbol{k})(v\boldsymbol{k}-\boldsymbol{q})}(\boldsymbol{G},\boldsymbol{q})\delta_{\sigma_{v'}\sigma_{c'}}\delta_{\sigma_c\sigma_v} \\
W_{ra'} &= \frac{1}{\Omega}\sum_{\boldsymbol{G}\boldsymbol{G'}} W_{\boldsymbol{G}\boldsymbol{G'}}(\boldsymbol{k'}-\boldsymbol{k}+\boldsymbol{q})(\rho_{\sigma_{v'}(v'\boldsymbol{k'}+\boldsymbol{q})(c\boldsymbol{k})}(\boldsymbol{G'},\boldsymbol{k'}-\boldsymbol{k}+\boldsymbol{q}))^{*}\times \\
&\quad\times\rho_{\sigma_{c'}(c'\boldsymbol{k'})(v\boldsymbol{k}-\boldsymbol{q})}(\boldsymbol{G},\boldsymbol{k'}-\boldsymbol{k}+\boldsymbol{q})\delta_{\sigma_{v'}\sigma_c}\delta_{\sigma_{c'}\sigma_v}
\end{aligned}
$$

Note that $\Omega = NV$ where N is equal to the number of $\boldsymbol{k}$ vectors considered in the FBZ, V is equal to the primitive cell volume, and f_M is equal to 2 in the case of non-magnetic calculations and to 1 in the case of magnetic calculations.

Screened potential

The screened potential can be obtained from the two following Hedin's equations:

$$W(1,2) = v(1,2) + \int d1'd2'v(1,1')\Pi(1',2')W(2',2) \tag{2.40}$$

$$\Pi(12) = -i\int d3d4\Gamma(134)G(23)G(42) \tag{2.41}$$

Introducing the dielectric function and the reducible polarizability χ:

$$\epsilon^{-1}(12) = \frac{1}{\delta(12) - \int d3v(13)\Pi(32)} = \delta(12) + \int d3v(13)\chi(32) \tag{2.42}$$

$$\chi(12) = \Pi(12) + \int d3d4\Pi(13)v(34)\chi(42) \tag{2.43}$$

the screened potential can be written in terms of the former quantities as:

$$W(12) = \int d3\epsilon^{-1}(13)v(32) \tag{2.44}$$

which after Fourier transformation becomes (considering the spatial periodicity of the system and the temporal static regime):

$$W_{\boldsymbol{G}\boldsymbol{G'}}(\boldsymbol{q}) = \epsilon^{-1}_{\boldsymbol{G}\boldsymbol{G'}}(\boldsymbol{q})v(\boldsymbol{q}+\boldsymbol{G'}) \tag{2.45}$$

where $v(\boldsymbol{q})$ ($v(\boldsymbol{q}) = \frac{e^2}{\epsilon_0}\frac{1}{|\boldsymbol{q}|^2}$ with dimension$[v] = eV\text{Å}^3$) is the Coulomb potential, with respectively:

$$\epsilon^{-1}_{\boldsymbol{GG'}}(\boldsymbol{q}\omega) = \delta_{\boldsymbol{GG'}} + v_{\boldsymbol{G}}(\boldsymbol{q})\chi_{\boldsymbol{GG'}}(\boldsymbol{q}\omega) \tag{2.46}$$

$$\sum_{\boldsymbol{G_1}}\left[\delta_{\boldsymbol{GG_1}} - \Pi_{\boldsymbol{GG_1}}(\boldsymbol{q}\omega)v_{\boldsymbol{G_1}}(\boldsymbol{q})\right]\chi_{\boldsymbol{G_1G'}}(\boldsymbol{q}\omega) = \Pi_{\boldsymbol{GG'}}(\boldsymbol{q}\omega) \tag{2.47}$$

At the random phase approximation (RPA) order, considering the generalized dipoles introduced above, the irreducible polarizability assumes the following form:

$$\Pi^0_{\boldsymbol{GG'}}(\boldsymbol{q}\omega) = \frac{1}{\Omega}\sum_{\sigma cv\boldsymbol{k}}(\rho_{\sigma(c\boldsymbol{k})(v\boldsymbol{k}-\boldsymbol{q})}(\boldsymbol{G},\boldsymbol{q}))^*\rho_{\sigma(c\boldsymbol{k})(v\boldsymbol{k}-\boldsymbol{q})}(\boldsymbol{G'},\boldsymbol{q})S_{cv\boldsymbol{k}\boldsymbol{q}\omega\sigma} \tag{2.48}$$

$$S_{cv\boldsymbol{k}\boldsymbol{q}\omega\sigma} = \left[\frac{1}{\omega + \epsilon_{v\sigma}(\boldsymbol{k}-\boldsymbol{q}) - \epsilon_{c\sigma}(\boldsymbol{k}) + i\eta} - \frac{1}{\omega + \epsilon_{c\sigma}(\boldsymbol{k}) - \epsilon_{v\sigma}(\boldsymbol{k}-\boldsymbol{q}) - i\eta}\right] \tag{2.49}$$

Absorption spectra at the Tamm-Dancoff approximation

From the excitonic eigenvalue E_λ and eigenvector A^λ (orthonormalized), we can build the oscillator strength of the excitonic state λ:

$$f^\lambda_\alpha = \sum_{\sigma cv\boldsymbol{k}}\rho_{\sigma(c\boldsymbol{k})(v\boldsymbol{k}-\boldsymbol{q_\alpha})}(\boldsymbol{0},\boldsymbol{q}_\alpha)(A^\lambda_{\sigma cv\boldsymbol{k}})^* \tag{2.50}$$

This allow us to express the macroscopic dielectric function as:

$$(\epsilon_M)_\alpha(\omega) = 1 - \lim_{q_\alpha\to 0}\frac{e^2}{2\epsilon_0|\boldsymbol{q}_\alpha|^2}\frac{1}{\Omega}\sum_\lambda\frac{f^\lambda_\alpha(f^\lambda_\alpha)^*}{\omega - E_\lambda} \tag{2.51}$$

where Ω is the primitive cell volume and α the direction of the electric field.

Absorption spectra beyond the Tamm-Dancoff approximation

From the excitonic eigenvalue E_λ and eigenvector A^λ, we can build the "direct" oscillator strength of the exciton state λ:

$$f^\lambda_{D\alpha} = \sum_{\sigma cv\boldsymbol{k}}\rho_{\sigma(c\boldsymbol{k})(v\boldsymbol{k}-\boldsymbol{q_\alpha})}(\boldsymbol{0},\boldsymbol{q}_\alpha)(A^\lambda_{\sigma cv\boldsymbol{k}})^* \tag{2.52}$$

and the "reverse" oscillator strength of the excitonic state λ:

$$f^\lambda_{R\alpha} = \sum_{\sigma cv\boldsymbol{k}}\rho_{\sigma(v\boldsymbol{k}+\boldsymbol{q})(c\boldsymbol{k_\alpha})}(\boldsymbol{0},\boldsymbol{q}_\alpha)(A^\lambda_{\sigma vc\boldsymbol{k}})^* \tag{2.53}$$

This allows us to express the macroscopic dielectric function as:

$$(\epsilon_M)_\alpha(\omega) = 1 - \lim_{q_\alpha\to 0}\frac{e^2}{2\epsilon_0|\boldsymbol{q}_\alpha|^2}\frac{1}{\Omega}\sum_{SS'\lambda\lambda'}\frac{f^\lambda_{S\alpha}M^{-1}_{\lambda\lambda'}(f^{\lambda'}_{S'\alpha})^*}{\omega - E_\lambda} \tag{2.54}$$

where α is the direction of the electric field and $M_{\lambda\lambda'} = \langle A^\lambda|A^{\lambda'}\rangle$.

Absorption spectra from a tight-binding Hamiltonian

The BSE approach relies on the calculation of the defined generalized dipole elements in eq. 2.37. These can be obtained directly from an electronic plane-wave calculation or from a generic tight-binding Hamiltonian. Let us describe the latter case when the Hamiltonian is defined in a orthogonal basis set

$$H_{ij}(\boldsymbol{R}\sigma) = \langle w_{i\sigma}\mathbf{0}|\,\hat{H}\,|w_{j\sigma}\boldsymbol{R}\rangle \tag{2.55}$$

where $|w_{i\sigma}\boldsymbol{R}\rangle$ is the basis set function i of the σ spin channel in the unit cell $\boldsymbol{R}$. A Fourier transform of the Hamiltonian allows us to consider only the basis set functions in the unit cell 0; in the collinear case, the Hamiltonians in the two spin channels are considered separately:

$$H_{ij}(\boldsymbol{k}\sigma) = \sum_{\boldsymbol{R}} H_{ij}(\boldsymbol{R}\sigma)e^{i\boldsymbol{k}\cdot\boldsymbol{R}} \tag{2.56}$$

This is a consequence of the Fourier transformation of its basis set

$$|w_{j\sigma}\boldsymbol{k}\rangle = \sum_{\boldsymbol{R}} |w_{j\sigma}\boldsymbol{R}\rangle\, e^{i\boldsymbol{k}\cdot\boldsymbol{R}} \tag{2.57}$$

The Hamiltonian is diagonalized in order to obtain Bloch states in the basis of the Fourier-transformed basis-set functions

$$H_{ij}(\boldsymbol{k}\sigma)\,|n\sigma\boldsymbol{k}\rangle = \epsilon_{n\sigma}(\boldsymbol{k})\,|n\sigma\boldsymbol{k}\rangle \tag{2.58}$$

$$\sum_j H_{ij}(\boldsymbol{k}\sigma)C_{j\sigma}^{n\boldsymbol{k}}\,|w_{j\sigma}\boldsymbol{k}\rangle = \epsilon_{n\sigma}(\boldsymbol{k})C_{i\sigma}^{n\boldsymbol{k}}\,|w_{i\sigma}\boldsymbol{k}\rangle \tag{2.59}$$

where $|n\sigma\boldsymbol{k}\rangle$ is the Bloch state n of the spin channel σ at the $\boldsymbol{k}$ point of the Brillouin zone, and $C_{j\sigma}^{n\boldsymbol{k}}$ is its projection over the j Fourier-transformed basis-set function of the Fourier-transformed basis set

$$|n\sigma\boldsymbol{k}\rangle = \sum_j C_{j\sigma}^{n\boldsymbol{k}}\,|w_{j\sigma}\boldsymbol{k}\rangle \tag{2.60}$$

$$= \sum_j C_{j\sigma}^{n\boldsymbol{k}} \sum_{\boldsymbol{R}} |w_{j\sigma}\boldsymbol{R}\rangle\, e^{i\boldsymbol{k}\cdot\boldsymbol{R}} \tag{2.61}$$

From the Bloch states in the two spin channels, a spinor is obtained

$$|n\boldsymbol{k}\rangle = |n\uparrow\boldsymbol{k}\rangle \otimes |n\downarrow\boldsymbol{k}\rangle = \sum_{i\uparrow} C_{i\uparrow}^{n\boldsymbol{k}}\,|w_{i\uparrow}\boldsymbol{k}\rangle \otimes \sum_{i\downarrow} C_{i\downarrow}^{n\boldsymbol{k}}\,|w_{i\downarrow}\boldsymbol{k}\rangle \tag{2.62}$$

The decomposition of the Bloch states into the basis set allows us to express the generalized dipole element defined above (Eq. 2.37) as

$$\rho_{\sigma(n1,\boldsymbol{k1})(n2,\boldsymbol{k2})}(\boldsymbol{G};\boldsymbol{p1},\boldsymbol{p2},\boldsymbol{q}) = \langle n1\boldsymbol{k1}-\boldsymbol{p1}|\,e^{i(\boldsymbol{q}+\boldsymbol{G})\cdot\boldsymbol{r}}\,|n2\boldsymbol{k2}-\boldsymbol{p2}\rangle$$
$$= \sum_{jl}\sum_{\boldsymbol{R}\boldsymbol{R'}} (C_{j\sigma}^{n1\boldsymbol{k1}-\boldsymbol{p1}})^* C_{l\sigma}^{n2\boldsymbol{k2}-\boldsymbol{p2}} e^{-i(\boldsymbol{k1}-\boldsymbol{p1})\cdot\boldsymbol{R}} e^{i(\boldsymbol{k2}-\boldsymbol{p2})\cdot\boldsymbol{R'}}\,\langle w_{j\sigma}\boldsymbol{R}|e^{i(\boldsymbol{q}+\boldsymbol{G})\cdot\boldsymbol{r}}|w_{l\sigma}\boldsymbol{R'}\rangle \tag{2.63}$$

where expressing the scalar product and doing the transformation $\boldsymbol{r'} = \boldsymbol{r} - \boldsymbol{R'}$ we obtain

$$\langle w_{j\sigma}\boldsymbol{R}|e^{i(\boldsymbol{q}+\boldsymbol{G})\cdot\hat{\boldsymbol{r}}}|w_{l\sigma}\boldsymbol{R'}\rangle = \int d\boldsymbol{r}(w_{j\sigma}(\boldsymbol{r}-\boldsymbol{R}))^* e^{i(\boldsymbol{q}+\boldsymbol{G})\cdot\boldsymbol{r}} w_{l\sigma}(\boldsymbol{r}-\boldsymbol{R'})$$
$$= \int d\boldsymbol{r}(w_{j\sigma}(\boldsymbol{r}+\boldsymbol{R'}-\boldsymbol{R}))^* e^{i(\boldsymbol{q}+\boldsymbol{G})\cdot(\boldsymbol{r}+\boldsymbol{R'})} w_{l\sigma}(\boldsymbol{r})$$

In the sum over $\boldsymbol{R'}$ we substitute $\boldsymbol{R}+\boldsymbol{R''}$, reducing the sum over $\boldsymbol{R}$ into the conservation law $\boldsymbol{k1}-\boldsymbol{p1} = \boldsymbol{k2}-\boldsymbol{p2}+\boldsymbol{q}$ and the rest to

$$\sum_{jl}(C_{j\sigma}^{n1\boldsymbol{k1}-\boldsymbol{p1}})^* C_{l\sigma}^{n2\boldsymbol{k2}-\boldsymbol{p2}} \sum_{\boldsymbol{R''}} e^{i\boldsymbol{q}\cdot\boldsymbol{R''}} \int d\boldsymbol{r}(w_{j\sigma}(\boldsymbol{r}+\boldsymbol{R''}))^* e^{i(\boldsymbol{q}+\boldsymbol{G})\cdot\boldsymbol{r}} w_{l\sigma}(\boldsymbol{r})$$

Thus, first the A element

$$A_{jl\sigma}(\boldsymbol{q},\boldsymbol{G},\boldsymbol{R''}) = \int d\boldsymbol{r}(w_{j\sigma}(\boldsymbol{r}+\boldsymbol{R''}))^* e^{i(\boldsymbol{q}+\boldsymbol{G})\cdot\boldsymbol{r}} w_{l\sigma}(\boldsymbol{r}) \tag{2.64}$$

is calculated (where the integral is discretized $\int d\boldsymbol{r} \to (V/N)\sum_l$, where N is the number of points; the Wannier functions are normalized in order to have modulus equal to 1 over the space grid). Then the M element

$$M_{jl\sigma}(\boldsymbol{q},\boldsymbol{G}) = \sum_{\boldsymbol{R''}} e^{i\boldsymbol{q}\cdot\boldsymbol{R''}} A_{jl\sigma}(\boldsymbol{q},\boldsymbol{G},\boldsymbol{R''}) \tag{2.65}$$

is calculated, and finally the generalized dipole element is calculated

$$\rho_{\sigma(n1,\boldsymbol{k1})(n2,\boldsymbol{k2})}(\boldsymbol{G};\boldsymbol{p1},\boldsymbol{p2},\boldsymbol{q}) = \langle n1\boldsymbol{k1}-\boldsymbol{p1}|\, e^{i(\boldsymbol{q}+\boldsymbol{G})\cdot\hat{\boldsymbol{r}}}\, |n2\boldsymbol{k2}-\boldsymbol{p2}\rangle$$
$$= \frac{(2\pi)^3}{V}\delta_{\boldsymbol{k1}-\boldsymbol{p1},\boldsymbol{k2}-\boldsymbol{p2}+\boldsymbol{q}} \sum_{jl}(C_{j\sigma}^{n1\boldsymbol{k1}-\boldsymbol{p1}})^* C_{l\sigma}^{n2\boldsymbol{k2}-\boldsymbol{p2}} M_{jl\sigma}(\boldsymbol{q},\boldsymbol{G})$$

We notice that while $\boldsymbol{k}_{1,2}$ represent grids of values covering the Brillouin zone, the points $\boldsymbol{p}_{1,2}$ and $\boldsymbol{q}$ are instead fixed throughout the BSE calculation.

The calculation of the dipole terms in real space can be very computationally demanding. An approximation is to assume δ-like basis-set functions, as done in [108]

$$A_{jl\sigma}(\boldsymbol{q},\boldsymbol{G},\boldsymbol{R''}) = \delta_{\boldsymbol{R''0}}\delta_{jl} e^{i(\boldsymbol{q}+\boldsymbol{G})\cdot\boldsymbol{r_i}} \tag{2.66}$$

where $\boldsymbol{r_i}$ is the center of the i-th basis-set function. Beside being quite naive, this approximation is partially predictive about optical gaps and relevant peaks. However, relevant dipole contributions are neglected. We will call it approximated-method (Eq. 2.64), to distinguish it from the complete-method (Eq. 2.63).

2.3.2 Magnetic excitations

In the case of magnetic systems, an addition has to be done: optical transitions involve transitions between occupied and empty states not related to spin-flipping processes. So when the H^{2p} is diagonalized, only the transitions preserving the spin momentum are considered. In fact, the transitions not preserving it are related to magnetic excitations: coherent ones and spin-flipping ones (Stoner continuum). Other ways to obtain the coherent spin excitations not through the BSE approach is through a mapping of

the ground-state results into an Heisenberg model and its diagonalization. The Heisenberg model is defined by the local magnetic moments of the system and the effective couplings between them:

$$\hat{H} = \frac{1}{2} \sum_{i,j;\alpha,\beta} J_{i,j}^{\alpha\beta} \hat{S}_i^{\alpha} \hat{S}_j^{\beta} \tag{2.67}$$

where i, j run over the magnetic atoms and α, β over the Cartesian coordinates, where $\hat{\boldsymbol{S}}$ is the atomic local magnetic moment, and $J_{i,j}$ the effective couplings between the pair of atomic magnetic moments (i, j).

The exchange coupling $J^{\alpha\beta}$ as a tensor of two indices can be decomposed into three parts (associating to each tensor index the SO(3) representation $l = 1$) [the Einstein notation is assumed]

$$\begin{aligned} 1 \otimes 1 &= 0 \oplus 1 \oplus 2 \\ J^{\alpha\beta} = \frac{1}{3} J^{\gamma\gamma} \delta^{\alpha\beta} + \frac{1}{2}(J^{\alpha\beta} - J^{\beta\alpha}) &+ \left[\frac{1}{2}(J^{\alpha\beta} + J^{\beta\alpha}) - \frac{1}{3} J^{\gamma\gamma} \delta^{\alpha\beta} \right] \\ J^{\alpha\beta} &= J\delta^{\alpha\beta} + \epsilon^{\alpha\beta\gamma} D^{\gamma} + K^{\alpha\beta} \end{aligned} \tag{2.68}$$

where the first term (0) is the isotropic Heisenberg exchange, the second term (1) the antisymmetric Dzyaloshinkii-Moriya interaction term, and the third term (2) the symmetric (anisotropic) Kitaev-type exchange. An additional term not contributing to the above exchange coupling is the single-ion anisotropy $A_i^{\alpha\beta}$, which with five indipendent components is a local site (i) term.

The interactions described by A, D and K originate from the spin-orbit coupling ($H = \lambda \hat{\boldsymbol{S}} \cdot \hat{\boldsymbol{L}}$), so in those system where the latter is not significant (because of quenching of the angular momentum), it is sufficient to consider only the isotropic interaction term J in the Heisenberg Hamiltonian.

The different exchange terms favour a different magnetic ordering of the local moments:

- A_i favours the alignment of the local moment along an easy-axis or in a easy-plane of the system
- $J_{i,j}$ favours parallel alignment of the moments i and j
- $D_{i,j}$ favours orthogonal alignment of the moments i and j
- $K_{i,j}$ favours parallel or anitparallel alignment of the moments i and j

Here, we underline the main steps of the derivation [109]. Local quantization frames can be defined in the magnetic ground state of the system for each magnetic atom. These frames have their local z component along the direction of the magnetic atom moment $\langle \hat{S} \rangle_i^{\alpha} = S\delta^{\alpha z}$ (in case of ground-state un-commensurate magnetic ordering, an additional local reference frame is defined with respect to the unit cells). Two additional vectors $(Re\{\boldsymbol{u}\}, Im\{\boldsymbol{u}\})$ define the plane orthogonal to the vector $\boldsymbol{v}$. The definition of the local reference frames allows us to map the magnetic ground state into a ferromagnetic ground state, for which annihilation and creation bosonic operators can be uniquely de-

fined using the Holstein-Primakoff transformations for all the magnetic atoms

$$\begin{aligned}
\hat{S}_i^z &= S - \hat{a}_i^\dagger \hat{a}_i \\
\hat{S}_i^+ &= \sqrt{2S}\sqrt{1 - \frac{\hat{a}_i^\dagger \hat{a}_i}{2S}}\hat{a}_i = \sqrt{2S}\left(1 - \frac{\hat{a}_i^\dagger \hat{a}_i}{4S}\right)\hat{a}_i + \dots \\
\hat{S}_i^- &= \sqrt{2S}\hat{a}_i^\dagger\sqrt{1 - \frac{\hat{a}_i^\dagger \hat{a}_i}{2S}} = \sqrt{2S}\hat{a}_i^\dagger\left(1 - \frac{\hat{a}_i^\dagger \hat{a}_i}{4S}\right) + \dots,
\end{aligned} \tag{2.69}$$

where the bosonic annihilation and creation operators satisfy the usual commutation relations

$$[\hat{a}_i, \hat{a}_j^\dagger] = \delta_{ij}, \quad [\hat{a}_i, \hat{a}_j] = 0, \quad [\hat{a}_i^\dagger, \hat{a}_j^\dagger] = 0. \tag{2.70}$$

Supposing an excited magnetic ground state $\langle \hat{a}_i^\dagger \hat{a}_i \rangle / S << 1$ with a number of magnetic excitations much smaller than the modulus of the local magnetic moment (small perturbations to the magnetic ground state), we can naively truncate the moment operator expansions above

$$\begin{aligned}
\hat{S}_i^z &= S - \hat{a}_i^\dagger \hat{a}_i \\
\hat{S}_i^+ &= \sqrt{2S}\hat{a}_i \\
\hat{S}_i^- &= \sqrt{2S}\hat{a}_i^\dagger
\end{aligned} \tag{2.71}$$

We are formally truncating the value of the Heisenberg Hamiltonian in the excited magnetic ground states $\langle \hat{H} \rangle$ neglecting interactions between the magnetic excitations.

In terms of the local reference frames defined above the truncated relations in equation 2.71 can be written as

$$\boldsymbol{S}_i = \sqrt{\frac{S_j}{2}}(\boldsymbol{u}_i a_i + \boldsymbol{u}_i a_i^\dagger) + \boldsymbol{v}_i(S_i - a_i^\dagger a_i) \tag{2.72}$$

where $(Re\{\boldsymbol{u}_i\}, Im\{\boldsymbol{u}_i\}, \boldsymbol{v}_i)$ is the local reference frame of the i-th magnetic atom, with local magnetic momentum in modulus equals to S_i.

After a Fourier transformation of the bosonic annihilation and creation operators (V is the unit cell volume)

$$\begin{aligned}
\hat{a}_i &= \frac{1}{\sqrt{V}} \sum_{\boldsymbol{k} \in \text{ B.Z.}} \hat{a}(\boldsymbol{k}) e^{i\boldsymbol{k}\cdot\boldsymbol{r}_i} \\
\hat{a}(\boldsymbol{k}) &= \frac{1}{\sqrt{V}} \sum_{i=1} \hat{a}_i e^{-i\boldsymbol{k}\cdot\boldsymbol{r}_i}
\end{aligned}$$

the following quadratic term of the Heisenberg Hamiltonian is obtained (a factor 2 is missing in the Heisenberg Hamiltonian of Ref. [109])

$$\hat{H} = \sum_{\boldsymbol{k} \in B.Z.} \hat{\boldsymbol{x}}^\dagger(\boldsymbol{k}) \cdot \boldsymbol{h}(\boldsymbol{k}) \cdot \hat{\boldsymbol{x}}(\boldsymbol{k}) = \sum_{\boldsymbol{k} \in B.Z.} \hat{\boldsymbol{x}}^\dagger(\boldsymbol{k}) \cdot \boldsymbol{h}(\boldsymbol{k}) \cdot \hat{\boldsymbol{x}}(\boldsymbol{k}) \tag{2.73}$$

where

$$\hat{\boldsymbol{x}}(\boldsymbol{k})^T = (\hat{a}_1(\boldsymbol{k}), \dots, \hat{a}_N(\boldsymbol{k}), \hat{a}_1^\dagger(-\boldsymbol{k}), \dots, \hat{a}_N^\dagger(-\boldsymbol{k})) \tag{2.74}$$

with the different components of the vector $\hat{\boldsymbol{x}}$ pointing to a different magnetic atom in the (magnetic) unit cell (N is the total number of magnetic atoms in the (magnetic) unit cell).

Let us consider the case of a ferromagnetic 3D crystal with one magnetic atom per unit cell. If the magnetic moment of the single atom is along the $\hat{z}$-direction, then the local reference frame can be written as

$$\boldsymbol{u}_i = (1, i, 0)^T \quad \boldsymbol{v}_i = (0, 0, 1)^T \tag{2.75}$$

Assuming no spin-orbit coupling, it follows that $J_{ij}^{\alpha,\beta}(\boldsymbol{k}) = 0$ when $\alpha \neq \beta$ and that $J^{\alpha} = J$ for $\alpha = x, y, z$ between any pair (i, j) of magnetic atoms. The Heisenberg Hamiltonian above, in equation (2.73), assumes then the following form (each entry of the matrix has dimension $N \times N$)

$$\begin{aligned}
\hat{H} = 2 \sum_{\boldsymbol{k}\in B.Z.} \sum_{ij} (\hat{\boldsymbol{x}}^{\dagger}(\boldsymbol{k}))_i \cdot \\
\cdot \begin{pmatrix} \frac{\sqrt{S_i S_j}}{2}(J^{xx}(-\boldsymbol{k}) + J^{yy}(-\boldsymbol{k}))_{ij} - R_{ij} & \frac{\sqrt{S_i S_j}}{2}(J^{xx}(-\boldsymbol{k}) - J^{yy}(-\boldsymbol{k}))_{ij} \\ \frac{\sqrt{S_i S_j}}{2}(J^{xx}(\boldsymbol{k}) - J^{yy}(\boldsymbol{k}))^*_{ij} & \frac{\sqrt{S_i S_j}}{2}(J^{xx}(\boldsymbol{k}) + J^{yy}(\boldsymbol{k}))^*_{ij} - R_{ij} \end{pmatrix} \cdot (\hat{\boldsymbol{x}}\boldsymbol{k}) \\
= 2 \sum_{\boldsymbol{k}\in B.Z.} \sum_{ij} (\hat{\boldsymbol{x}}^{\dagger}(\boldsymbol{k}))_i \cdot \\
\cdot \begin{pmatrix} \frac{\sqrt{S_i S_j}}{2}(J^{xx}(-\boldsymbol{k}) + J^{yy}(-\boldsymbol{k}))_{ij} - R_{ij} & 0_{ij} \\ 0_{ij} & \frac{\sqrt{S_i S_j}}{2}(J^{xx}(\boldsymbol{k}) + J^{yy}(\boldsymbol{k}))^*_{ij} - R_{ij} \end{pmatrix} \cdot (\hat{\boldsymbol{x}}(\boldsymbol{k}))_j \\
= 2S \sum_{\boldsymbol{k}\in B.Z.} \sum_{a} \Big((J(-\boldsymbol{k}) - J(\boldsymbol{0}))\hat{a}_i^{\dagger}(\boldsymbol{k})\hat{a}_i(\boldsymbol{k}) - (J(-\boldsymbol{k}) - J(\boldsymbol{0}))\hat{a}_i^{\dagger}(-\boldsymbol{k})\hat{a}_i(-\boldsymbol{k}) \Big) \\
+2S \sum_{\boldsymbol{k}\in B.Z.} (J(-\boldsymbol{k}) - J(\boldsymbol{0}))
\end{aligned}$$

Lastly, being the Heisenberg Hamiltonian already diagonal, we can directly consider the positive energy solutions, and neglect the last constant term (zero point energy)

$$\hat{H}|_p = 2S \sum_{\boldsymbol{k}\in B.Z.} (J(-\boldsymbol{k}) - J(\boldsymbol{0}))\hat{a}^{\dagger}(\boldsymbol{k})\hat{a}(\boldsymbol{k}) \tag{2.76}$$

the magnonic dispersion relation directly follows

$$\omega(\boldsymbol{k}) = 2S(J(-\boldsymbol{k}) - J(\boldsymbol{0})) = 2S \sum_{\boldsymbol{d}} J(\boldsymbol{d})(e^{i\boldsymbol{k}\cdot\boldsymbol{d}} - 1) \tag{2.77}$$

where $\boldsymbol{d}$ is the distance between two magnetic atoms (in terms of unit cells). Assuming isotropic first-nearest-neighborhood (case of a simple cubic crystal) interaction, we obtain the usual ferromagnetic solution [110]

$$\omega(\boldsymbol{k}) = 2SJ \sum_{\boldsymbol{d}} (e^{i\boldsymbol{k}\cdot\boldsymbol{d}} - 1) = 12SJ \left(\frac{1}{3}(\cos(k_x L) + \cos(k_y L) + \cos(k_z L)) - 1 \right) \tag{2.78}$$

where L is the lattice parameter.

The diagonalization of $h(\boldsymbol{k})$ is usually performed through the Colpa's method in order to preserve the commutation relations [111].

We now present two methods that can be used to evaluate the exchange couplings.

Extraction of the exchange couplings: energy method

Different magnetic orderings are considered at the DFT level and the energies matched to the corresponding Heisenberg Hamiltonians. This is done in order to obtain a system of equations, with unknowns the exchange couplings.

For example, let us consider a 1D chain of magnetic atoms (one atom per unit cell) and calculate the next nearest neighbor (NNN) exchange couplings. In order to calculate the next nearest neighbor coupling a unit cell containing three atoms is required (atom 0, atom 1 and atom 2). The system obtained is the following:

$$E_{\uparrow\uparrow\uparrow} = J_{01} + J_{02} + J_{12} + E_0 \tag{2.79}$$
$$E_{\uparrow\downarrow\uparrow} = -J_{01} + J_{02} - J_{12} + E_0 \tag{2.80}$$
$$E_{\uparrow\downarrow\downarrow} = -J_{01} - J_{02} + J_{12} + E_0 \tag{2.81}$$
$$E_{\downarrow\downarrow\uparrow} = J_{01} - J_{02} - J_{12} + E_0 \tag{2.82}$$

where the $\uparrow, \downarrow$ indicate the magnetic momentum orientations of the single atom, E_0 the energy not related to the magnetic exchange coupling and the $E_{\sigma_1\sigma_2\sigma_3}$ the DFT energies associated to the particular magnetic configuration. This system can be solved in terms of the unknown exchange couplings, inverting the corresponding matrix:

$$J_{01} = (1/4)(E_{\uparrow\uparrow\uparrow} - E_{\uparrow\downarrow\uparrow} - E_{\uparrow\downarrow\downarrow} + E_{\downarrow\downarrow\uparrow}) \tag{2.83}$$
$$J_{02} = (1/4)(E_{\uparrow\uparrow\uparrow} + E_{\uparrow\downarrow\uparrow} - E_{\uparrow\downarrow\downarrow} - E_{\downarrow\downarrow\uparrow}) \tag{2.84}$$
$$J_{12} = (1/4)(E_{\uparrow\uparrow\uparrow} - E_{\uparrow\downarrow\uparrow} + E_{\uparrow\downarrow\downarrow} - E_{\downarrow\downarrow\uparrow}) \tag{2.85}$$
$$E_0 = (1/4)(E_{\uparrow\uparrow\uparrow} + E_{\uparrow\downarrow\uparrow} + E_{\uparrow\downarrow\downarrow} + E_{\downarrow\downarrow\uparrow}) \tag{2.86}$$

Extraction of the exchange couplings: magnetic force theorem method

Small variations of the moment configurations with respect to the magnetic ground state can be related trough the magnetic force theorem to variations of occupied single-particle states [112–115].

This relation allows one to obtain the exchange coupling dependence from the real-space Green's functions ($G_{ij}(\epsilon)$ Fourier transform in time of equation 2.25) and the local interaction of a site with itself, $H_{ii}(\boldsymbol{R} = 0)$. Defining $\Delta_i = H^{\uparrow}_{ii}(\boldsymbol{R} = 0) - H^{\downarrow}_{ii}(\boldsymbol{R} = 0)$, we have

$$J_{ij} = \frac{1}{4\pi} \int_{-\infty}^{E_F} ImTr\left\{ \Delta_i G^{\uparrow}_{ij} \Delta_j G^{\downarrow}_{ji} \right\} \tag{2.87}$$

where J_{ij} is the isotropic exchange coupling and E_F the Fermi energy.

In the following results, a procedure called downfolding method [116] is used, in order to include the ligand atoms contributions to the interaction parameters between the (localized) not-ligand atoms

$$\tilde{J}_{TT} = J_{TT} - J_{TL} * [J_{LL}]^{-1} J_{LT} \tag{2.88}$$

Although this procedure can give inconsistent results when applied to an approximated theory as the one of the MFT [116], it performs sufficiently well in the case of NiO. As the molecule does not significantly couple with the substrate, the addition of its atoms to the downfolding does not give any major contribution, assuring us of the suitability of this method also for the adsorbed system.

Wannier functions

In order to use the formalism of magnetic force theorem method, our DFT reciprocal-space results have to be translated into a real-space language, having expressed the exchange couplings in terms of Green's functions in real-space 2.87.

We can choose the set of functions that span the band space or any N-branch band space (a set of N bands) (with some exceptions on the properties of the set of functions). Bloch functions or any combination of them (generalized Bloch functions):

$$\psi_{n\boldsymbol{k}}(\boldsymbol{r}) = \sum_{m}^{N} U_{nm}(\boldsymbol{k})\psi_{m\boldsymbol{k}}(\boldsymbol{r}) \tag{2.89}$$

where $U_{nm}(\boldsymbol{k})$ is a non-singular matrix, constitute one choice, that is local in $\boldsymbol{k}$-space. Real space orbitals $a_i(\boldsymbol{r})$ constitute a different choice, which instead is local in $\boldsymbol{r}$-space

$$\psi_{j\boldsymbol{k}}(\boldsymbol{r}) = \sum_{i}^{N} T_{ji}(\boldsymbol{k})a_i(\boldsymbol{r} - \boldsymbol{R_i}) \tag{2.90}$$

where $T_{ji}(\boldsymbol{k})$ is a non-singular matrix. As real-space orbitals to describe the r-branch band space, the Fourier transforms of the generalized Bloch functions can be considered

$$w_{n\boldsymbol{R}}(\boldsymbol{r}) = \int_{BZ} \frac{d\boldsymbol{k}}{(2\pi)^3} e^{i\boldsymbol{k}\cdot\boldsymbol{R}} \sum_{m}^{N} U_{nm}(\boldsymbol{k})\psi_{m\boldsymbol{k}}(\boldsymbol{r}) \tag{2.91}$$

where $\boldsymbol{R}$ is the conjugate variable of the momentum $\boldsymbol{k}$. These are commonly known as Wannier functions (WF); if we are interested in localized Wannier functions, which are commonly known as Maximally Localized Wannier functions (MLWF), instead, it is necessary to properly choose the matrices $U_{nm}(\boldsymbol{k})$ which combine the Bloch functions, for example by minimising the sum of the quadratic spreads of the WFs about their centres

$$\Omega[\boldsymbol{r}] = \sum_{n=1}^{N} \left[\langle w_{n\boldsymbol{0}}|\boldsymbol{r}\cdot\boldsymbol{r}|w_{n\boldsymbol{0}}\rangle - |\langle w_{n\boldsymbol{0}}|\boldsymbol{r}|w_{n\boldsymbol{0}}\rangle|^2 \right] \tag{2.92}$$

2.4 Computational details

In the following we underline the codes implemented for this work and the existing codes used in the different calculations.

2.4.1 DFT calculations

We evaluate the ground state of the studied systems and their properties using DFT in a plane-waves basis set, as implemented in the Quantum ESPRESSO distribution (6.8,7.2) [117, 118]. Hubbard corrections are included in their Dudarev formulation (a single parameter is given $U_{eff} = U - J$) to correct for self interaction error. Due to the low symmetry of the studied systems this correction improves capturing some aspects of correlation. The values considered, $U_{\text{Co,Ni,Cr}} = 4.0$ eV and $U_{\text{Fe}} = 5.0$ eV, were chosen following the literature so as to optimize the electronic properties (density of states) of the localized orbitals for the isolated systems [12, 119]. We evaluated self-consistently the U value in the case of NiO using Density Functional Perturbation theory (DFPT) [120],

obtaining a result of 7.99 eV comparable to the one already reported in analogue calculations [121]. The experimental comparison approach in this case seems more predictive than more refined approaches.

We include the van der Waals interactions between the molecule and the substrate by using the vdW-DF-C09 exchange and correlation (xc) functional [122, 123]. Vanderbilt ultrasoft pseudopotentials (GBRVs) [124] with semicore corrections are used, selecting a plane wave cutoff of 45 Ry for the wave functions and of 270 Ry for the charge density. In case of supercells the surface Brillouin zone is sampled by the Γ point only. Comparing the total energy of a 1×1 cell and of the corresponding supercell, considering respectively a grid of $8 \times 8 \times 8$ k points and a Γ point to cover the Brillouin zone, a convergence is obtained in the order of 2×10^{-3} eV/atom for the CoO(001) and NiO(001), and in the order of 5×10^{-5} eV/atom for the Cr_2O_3(0001). The substrates are modeled with a slab that includes a variable number of layers. The number of layers is defined by the necessity to have partial convergence of the surface states to bulk states. Equilibrium geometries are obtained through a structural optimization of the molecule and of the top layers of the substrates.

2.4.2 Optical spectra calculations

The optical spectra of the studied systems are associated with the 2D polarizability, obtained through the imaginary part of the dielectric function (eq. 2.42). This is evaluated at the independent particle (IPA) level through the matrix elements of the dipole operator between the Kohn–Sham states. These calculations were performed using the Yambo code (5.1) [125], a plane-wave code interfaced with Quantum ESPRESSO. Since Yambo is not compatible with ultrasoft pseudopotentials or with VdW-DF-C09 exchange correlation functionals, additional calculations at fixed atomic coordinates were performed with norm-conserving pseudopotentials (Pseudo-Dojo [126]) and the Perdew–Burke–Ernzerhof (PBE) [127] exchange correlation, including as well the Hubbard corrections as specified above. We verified the consistency of the electronic and magnetic structure with those obtained before. In the dielectric function evaluation, we considered the Hubbard correction to the Kohn–Sham eigensystem as described above, but we computed approximate matrix elements by neglecting the contribution by the Hubbard Hamiltonian while evaluating the commutator $[r, H]$.

The optical spectra of the spinterfaces are then analysed through a projection of the valence and conduction states characterizing each transition, over the atomic orbitals of each atom, in order to single out the "molecular contributions" of the transitions. For each transition we sum the squared projections of the valence/conduction states involved ψ_v on the atomic orbitals ϕ_{nlm} of the atom J

$$w_v^{(J)} = \sum_{nlm} |\, \langle \phi_{nlm}^{(J)} | \psi_v \rangle \,|^2 \tag{2.93}$$

where J is one of the atoms of the molecule. This sum is then weighted by the transition intensity I_t. The transitions with similar energies, are grouped into bins b (a binning of 0.05 eV has been chosen), so that the molecular projection is given within a bin as

$$P_b^{(v/c)} = \left\{ \sum_{t\in b} I_t \left[\sum_{J\in FePc} w_{v/c(t)}^{(J)} \right] \right\} / \left\{ \sum_{t\in b} I_t \right\} \tag{2.94}$$

As a further analysis, following an analogue route as the one above, we evaluate the localization of the charge with respect to the normal to the surface of the Kohn-Sham

states contributing to the optical transitions in a given bin

$$z_b^{(v/c)} = \left\{ \sum_{t\in b} I_t \left[\sum_{J\in FePc} z^{(J)} w_{v/c(t)}^{(J)} \right] \right\} / \left\{ \sum_{t\in b} I_t \right\} \tag{2.95}$$

This allows us to partially quantify the movement along the normal to the surface of the electrons before and after the optical excitation, taking as a reference (z = 0) the height of top-surface atoms.

In case of the isolated molecule we evaluated as well the optical spectra at the BSE order, after the addition of G0W0 corrections (one cycle of the Hedin's equation in the GW approximation 2.30). In this case the xc-functionals used are instead the hybrids PBE0 [128].

2.4.3 Magnons calcuations

A wannierisation procedure performed by the code Wannier90 [129] allows us to extract from the DFT results a tight-binding model of the system. This is then used in a perturbative approach based on magnetic force theorem (MFT), to extract the exchange couplings of an Heisenberg model 2.67 trough the use of the TB2J code [114]. Only collinear terms have been considered. A downfolding is applied in the extraction of the exchange couplings, due to the presence of the ligands atoms in the substrate. At this point, a Holstein-Primakoff transformation of the spin operator in the Heisenberg model allows us to introduce annihilation/creation operators of quasiparticle quanta, i.e. magnons, and to extract from the Heisenberg model their dispersion law through a diagonalization procedure (Colpa's method) [111]. The diagonalization procedure is done using the Magnon code implemented for this work, and described in the next section.

2.4.4 Implemented codes

Magnon code

The code follows the structure of the reference [109]. A local frame is defined with respect to each magnetic atom. Than the Heisenberg Hamiltonian is built taking into account the local reference frames. Then thorugh the Colpa's method [111] the Hamiltonian is diagonalized. The code is inside the "Magnons" repository of my github account marcomarino123 [130], is written in C/C++ and uses Lapack libraries for the diagonalization or Cholesky factorization routines. The following classes have been implemented with relative methods:

- Crystal
- Spin
- Lattice of Spins
- Lattice of Exchange Couplings
- Heisenberg Hamiltonian
- Lattice of K points
- (Berry Curvature)

The code takes from input the crystal structure (Bravais lattice and basis), the magnetic ground state, and the magnetic couplings between pairs of atoms. The magnetic ground state is defined by the magnetic moment vectors for each atom of the basis. The J couplings are defined in real space and for different pairs of atoms (ij) in different unit cells (d is the distance between the unit cells); in this regard, a threshold on the distance can be set. The $J_{ij}(\boldsymbol{d})$ couplings are Fourier transformed according to

$$J_{ij}(\boldsymbol{k}) = \sum_{\boldsymbol{d}} J_{ij}(\boldsymbol{d}) e^{i\boldsymbol{d}\cdot\boldsymbol{k}} \tag{2.96}$$

The couplings are stored (for each $\boldsymbol{d}$ or $\boldsymbol{k}$) in 4-dimensional arrays $J(i,j,k,l)$ where (ij) refers to the pair of atoms, while (kl) to the direction of the coupling $k,l = x,y,z$. Because of this definition, the inclusion of magnetic anisotropies is quite straightforward: it is necessary to slightly modify the input reading routine of the J couplings. The Heisenberg Hamiltonian is built according to [109], except for a factor 2 missing in Eq. 2.97

$$\hat{H} = \sum_{\boldsymbol{k}\in BZ} \hat{\boldsymbol{x}}(\boldsymbol{k})^\dagger \cdot \boldsymbol{h}(\boldsymbol{k}) \cdot \hat{\boldsymbol{x}}(\boldsymbol{k}) \tag{2.97}$$

where $\hat{\boldsymbol{x}}$ can be written in terms of the Fourier transformed bosonic annihilation/creation operators associated to each magnetic atom (N is the number of magnetic atoms per unit cell) as

$$\hat{\boldsymbol{x}}(\boldsymbol{k}) = [a_1(\boldsymbol{k}), \ldots, a_N(\boldsymbol{k}), a_1^\dagger(-\boldsymbol{k}), \ldots, a_N^\dagger(-\boldsymbol{k})]^T \tag{2.98}$$

while $\boldsymbol{h}$ can be written as

$$\boldsymbol{h}(\boldsymbol{k}) = \begin{pmatrix} \boldsymbol{A}(\boldsymbol{k}) - \boldsymbol{C} & \boldsymbol{B}(\boldsymbol{k}) \\ \boldsymbol{B}(\boldsymbol{k})^\dagger & \boldsymbol{A}^*(-\boldsymbol{k}) - \boldsymbol{C} \end{pmatrix} \tag{2.99}$$

where A, B, C are $N \times N$ matrix and to each magnetic atom is associated a local reference frame $(\boldsymbol{u}_i, \boldsymbol{v}_i)$)

$$\begin{aligned} (A(\boldsymbol{k}))_{ij} &= \frac{\sqrt{S_i S_j}}{2} \boldsymbol{u}_i^T J_{ij}(-\boldsymbol{k}) \boldsymbol{u}_j^* \\ (B(\boldsymbol{k}))_{ij} &= \frac{\sqrt{S_i S_j}}{2} \boldsymbol{u}_i^T J_{ij}(-\boldsymbol{k}) \boldsymbol{u}_j \\ (C(\boldsymbol{k}))_{ij} &= \delta_{ij} \sum_l S_l \boldsymbol{v}_i^T J_{ij}(\boldsymbol{0}) \boldsymbol{v}_l \end{aligned}$$

The Heisenberg Hamiltonian is then Cholesky factorized and properly multiplied by the matrix $((\boldsymbol{10})(\boldsymbol{0}-\boldsymbol{1}))$ in order to make it positive definite (Colpa's method [111]). Lastly it is diagonalized and again multiplied by the matrix $((\boldsymbol{10})(\boldsymbol{0}-\boldsymbol{1}))$; the positive solutions are then the magnons. This is done for each $\boldsymbol{k}$ point.

Wannier+BSE code

The code follows the structure of the subsection 2.3.1 of this chapter: for each quantity a class with its methods and attributes has been defined. The code is inside the "BSE" repository of my github account marcomarino123 [131], is written in C/C++ and uses the Armadillo [132] and the OpenMP libraries [133].

The following classes have been implemented with relative methods:

- Crystal lattice
- Lattice of k points
- G points
- tight-binding Hamiltonian
- Wannier Function in real space
- Coulomb potential
- Generalized dipole element (delta-like Wannier functions + real-space integrals)
- Dielectric function
- Excitonic Hamiltonian (resonant part + coupling part + spin transformations + macroscopic dielectric function + cut-off W interaction (passing through dipoles))

The code takes in input the crystal structure and the basis. Moreover, if the dipoles are calculated in the approximated way, the Wannier function centers are also required, while if the dipoles are calculated by real space integrals, the Wannier functions in real space are required. The dielectric function can be calculated at the RPA level, as the W screening potential. Electronic bands can be extracted from the tight-binding Hamiltonian. The excitonic Hamiltonian can be built at the Tamm-Dancoff level or beyond. Magnetic calculations can be considered as well. In the case of magnetic calculations, spinors are built and the excitonic Hamitlonian is decomposed into its singlet and triplet spin transitions; in fact, spin-flip transitions as magnonic excitations can be extracted as well. Non-local corrections can be included.

The code is under testing, this thesis includes only some preliminary results. See Appendix B.

Part II
Fe-phthalocyanine

CHAPTER 3

Fe-phthalocyanine

In this chapter we study the Fe-phthalocyanine from an energetic, magnetic and optical point of view. The energetic studies emphasize the presence of a Jahn-Teller deformation ($D_{4h} \rightarrow D_{2h}$). The magnetic studies underline an opposite magnetization of the Fe atom and the N atoms around. The optical studies highlight charge accumulation in the center of the molecule.

3.1 Literature review

Among the variety of molecular compounds, organo-metallic ones offer the favour of facilitating a magnetic coupling with the substrate. Mainly studied in the perspective of catalytic activity [134, 135], there are related studies in the field of spintronics about chemical switching of surface-induced magnetic ordering [136–138], or not-related, only about surface-induced magnetic ordering [139].

Fe-phthalocynanine as an intermediate-spin open-shell system, may possess highly structured potential energy surfaces [140], consequence of the closeness in energy of several electronic configurations. In this regard, in fact, there are studies about its ground state [8, 141, 142], which demonstrate how the DFT calculations are significantly dependent on the exchange-correlation functionals used (Fig. 3.1) or the basis sets used.

These studies, however, do not investigate the possibility of a distortion of the molecule, which is assumed to preserve its D_{4h} symmetry, and a Jahn-Teller distortion is related to artifactual symmetry breaking [143]. In our case, the asymmetric wavefunction in the structural distorted configuration has lower energy than the symmetric one or asymmetric one in the structural undistorted configuration, assuring us of the reality of the Jahn-Teller distortion.

As we will show in this chapter, the breaking of the symmetry is a relevant feature in terms of obtaining the proper ground-state, underlining that a major effort also in this regard is needed.

Moreover to consider methods more accurate than DFT, would result in a better description of the features of the isolated molecule, but at the same time would make the spinterface problem numerically intractable.

3.2 Computational details

The ground-state and its properties are evaluated using DFT in a plane-waves basis set (Quantum ESPRESSO [117, 118]). Different exchange-correlation potentials have been used: PBE [144], with van der Waals corrections (vdW-DF-C09 [122, 123]), PBE0 [128]. Hubbard corrections, when indicated, are included, in their Dudarev's formulation (a

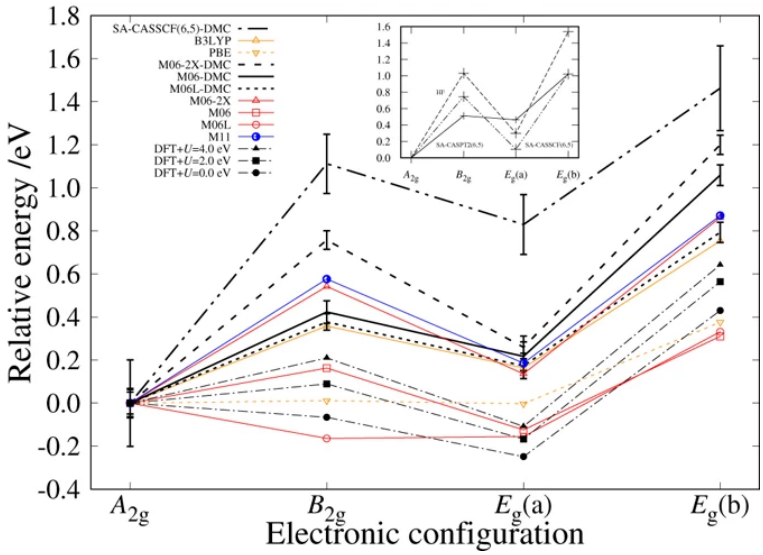

Figure 3.1 The predictions of some ab initio methods. This graph shows the predictions of CASSCF-DMC, DFT-DMC, HF, CASSCF, CASPT2, and some DFT calculations about the relative stability among the four electronic configurations: $A_{2g}[(d_{z2})^{\uparrow\downarrow}(d_{xz},d_{yz})^{\uparrow\downarrow}(d_{xy})^{\uparrow\downarrow}]$, $B_{2g}[(d_{z2})^{\uparrow}(d_{xz},d_{yz})^{\uparrow\downarrow\uparrow\downarrow}(d_{xy})^{\uparrow}]$, $E_g(a)[(d_{z2})^{\uparrow}(d_{xz},d_{yz})^{\uparrow\downarrow\uparrow}(d_{xy})^{\uparrow\downarrow}]$ and $E_g(b)[(d_{z2})^{\uparrow\downarrow}(d_{xz},d_{yz})^{\uparrow\downarrow\uparrow}(d_{xy})^{\uparrow}]$. Reproduced from [8].

single parameter is given $U_{eff} = U - J$), to describe on-site correlation effects of the transition-metal atom (Fe). Different U values have been considered, but the preferential one is $U_{Fe} = 5.0$ eV, being the one, following the literature [145, 146], able to optimize the electronic properties (density of states) of the localized orbital. Vanderbilt ultrasoft pseudopotentials (GBRV) [124] with semi-core corrections are generally used, selecting a plane wave cutoff of 45 Ry for the wavefunctions and of 270 Ry for the charge density. In the case of PBE0 calculations, PBE0-related norm-conserving scalar-relativistic pseudopotentials are considered instead, selecting a plane wave cutoff of 95 Ry for the wavefunctions and of 220 Ry for the charge density (here we have done some testing on the convergence, which showed us we could significantly reduce the cutoff for the charge density). A sufficiently large supercell has been considered to avoid interactions between the periodic images of the molecule. As an isolated system, Γ point sampling of the Brillouin zone is considered. To notice is the fact that our calculations do not include any spin-orbit coupling, which could induce a mixing of the possible ground-state configurations [147], increasing the possibilities of ground-state configurations.

3.3 Structural properties

In Fig. 3.2 we show the structure of the Fe-phthalocyanine. A relaxation (with ultrasoft pseudo-potentials (GBRV)) using PBE xc-functionals, and one considering on top of that VdW and Hubbard corrections (U parameter of 5.00 eV), give similar molecular structural characteristics, as reported in Table 3.1.

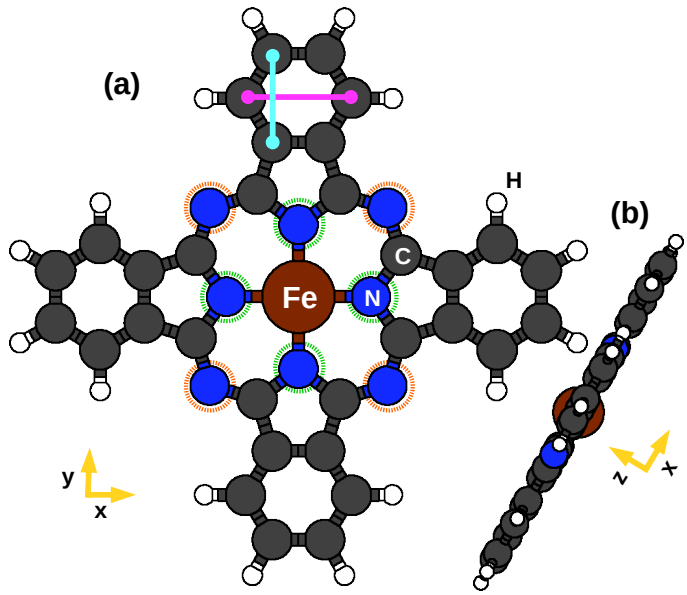

Figure 3.2 (a) front view of the Fe-phthalocyanine molecule; (b) side view of the Fe-phthalocyanine molecule. Color scheme as follows. Brown: Fe; Blue: N; Dark-gray: C; White: H. Circled in Orange: imide N atoms, circled in Green: pyrrolic N atoms. The Light-blue line: C-C distance in the phenyl-ring along y (C-C-y); the Purple line: C-C distance in the phenyl-ring along x (C-C-x).

Table 3.1 Structural properties of Fe-phthalocyanine obtained after a structural relaxation of the molecule . Here the U value considered in the Dudarev's formulation is 5.00 eV.

	PBE	PBE+U+VdW [Å]
Fe - pyrrolic N	1.93	1.94
Fe - imide N	3.38	3.38
C - C - x	2.85	2.85
C - C - y	2.39	2.38

The similar values given by the two numerical setups show how in the case of a single U-corrected atom, the structure is not significantly affected by the U correction. Moreover, the F-pyrrolic N atom distance well reproduces the experimental value of 1.93 Å [145].

3.4 Influence of the Hubbard parameter

Interested in the effects on the electronic structure of the choice of a specific effective Hubbard value, we have systematically varied the U-parameter using the PBE relaxed geometry. As we will see better in the following sections this structure has a very small asymmetry, which breaks the D_{4h} symmetry in favour of a D_{2h} symmetry, allowing asymmetric electronic solutions: a difference of 0.01 Å between the two orthogonal distances between the Fe atom and the two pyrrolic N atoms. In Fig. 3.3 we report the total energy at varying U values; the one with an extremely small U ($< 10^{-4}$ eV) value is taken as a reference.

From the curve and its discontinuities, it can be deduced that the molecule can have different electronic configurations. We expect that these are mainly related to the atomic configuration of the Fe atom, due to the fact that the U parameter is acting directly on its populations. We took a look at the electronic charge density, polarization (Table 3.2), and Löwdin populations (Table 3.3) of the Fe atom for three near-by U values of different molecular electronic configurations (Blue square in Fig. 3.3). The B configuration

Table 3.2 Electronic charge and polarization of the Fe atom, for different U values of the Hubbard correction and for different molecular phases, indicated by the letters: A, B and C. The ρ are in terms of the number of electrons, while μ are in units of μ_B.

U [eV]	ρ (s)	ρ (p)	ρ (d)	μ (s)	μ (p)	μ (d)
4.75 (A)	2.48	6.98	6.22	0.093	0.003	2.460
5.00 (B)	2.48	6.95	6.34	0.094	0.024	2.045
5.25 (C)	2.47	6.94	6.34	0.094	0.023	2.135

at lower energy is the only one among the configurations which is breaking the D_{4h} symmetry. This solution having the same symmetry as the structure D_{2h} (as underlined above) is the proper ground-state [140]. The structural and electronic breaking of the symmetry is a sign of the Jahn-Teller effect. The B configuration as we will see in the following section, is not stable in the case of a completely symmetrical structure of the molecule, underlining even more that the Jahn-Teller effect we are seeing is not a pseudo one due to the low accuracy of our calculations, but a real one. The C configuration has a different filling of the d orbitals with respect to the A configuration. Quite interesting,

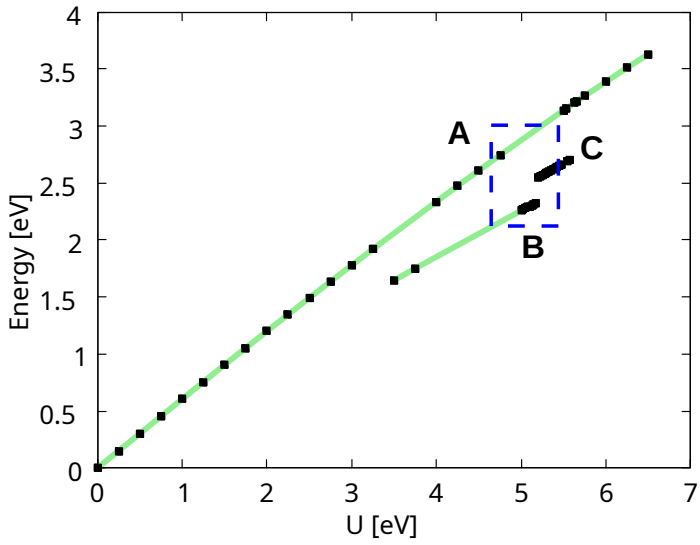

Figure 3.3 Fe-phthalocyanine SCF studies at varying effective U parameter in the Hubbard correction. Calculations done with PBE+U+VdW and ultrasoft pseudopotentials (GBRV). In letters three electronic configurations of the Fe electronic structure are underlined.

Table 3.3 Löwdin populations of the Fe atom $(m_\uparrow, m_\downarrow)$, for different U values of the Hubbard correction and for different molecular configurations, indicated by the letters: A, B and C. The populations are in terms of the number of electrons.

U [eV]	dz2	dxz	dyz	dx2-y2	dxy
4.75 (A)	↑ (0.96,0.03)	↑ (0.98,0.30)	↑ (0.98,0.30)	(0.45,0.28)	↑↓ (0.98,0.96)
5.00 (B)	↑ (0.95,0.03)	↑↓ (0.95,0.89)	↑ (0.97,0.03)	(0.36,0.25)	↑↓ (0.97,0.96)
5.25 (C)	↑ (0.95,0.02)	↑↓ (0.95,0.89)	↑↓ (0.95,0.89)	(0.40,0.27)	↑ (0.98,0.02)

the B configuration is naturally obtained for the U value suggested from the literature [145, 146]. For completeness, we can also have a look at the DOS projected on the Fe d orbitals, for the two spin-channels and for the different U values, in Fig. 3.4.

The presence of the three different configurations A, B and C, emerges from the discontinuous transitions of the d populations.

3.5 Comparison to hybrid functionals

The accuracy of the DFT+U description has been evaluated through a calculation using Hybrids exchange-correlation functionals. The PDOS of the two calculations is reported in Fig. 3.5, while the electronic populations of the Fe atom is reported in Table. 3.4.

From this comparison, we conclude that the DFT+U calculations are able to reproduce the Fe electronic populations, as well as the rest of the molecule states near Fermi,

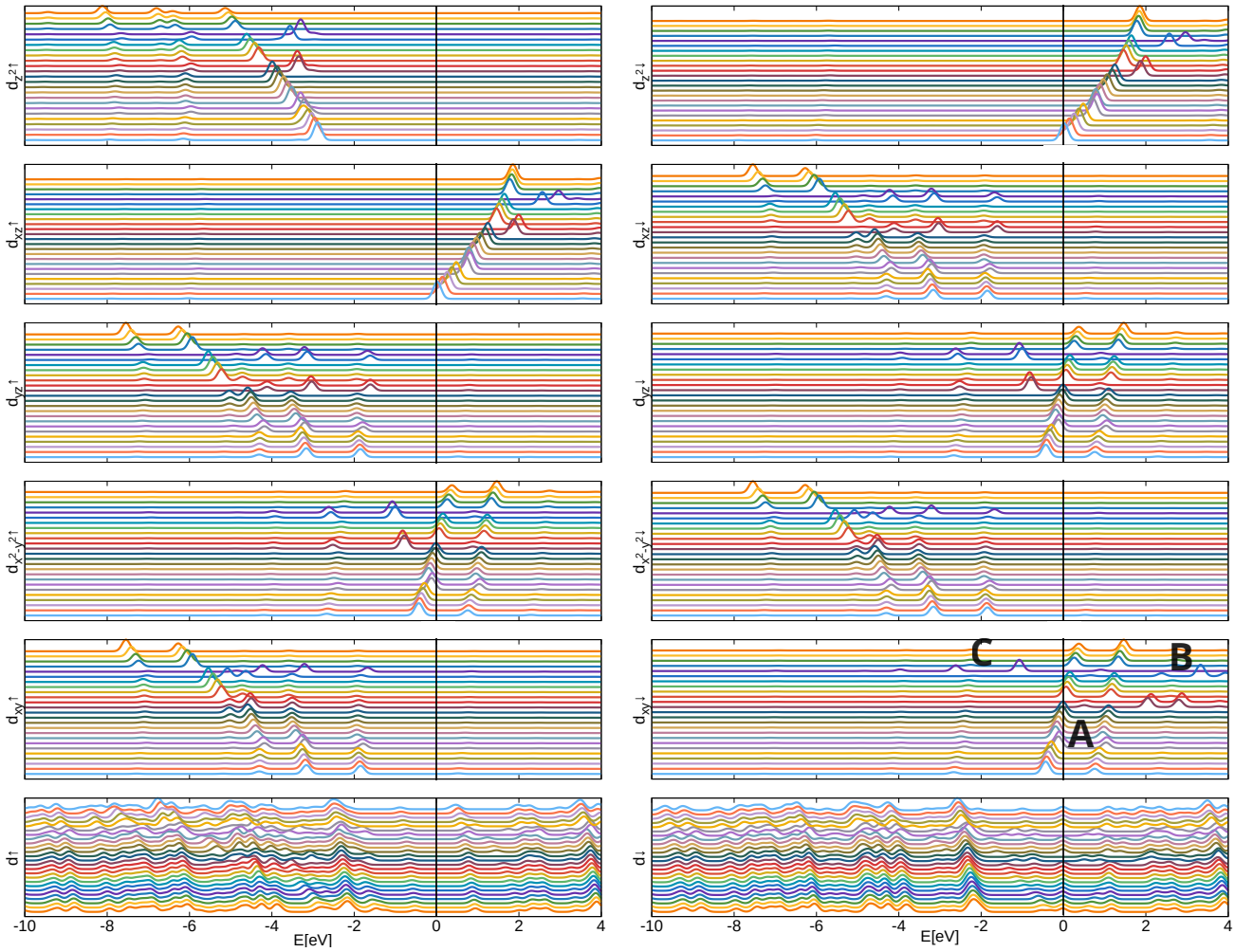

Figure 3.4 PDOS of the Fe-phthalocyanine over the Fe d orbitals for different U values in the range from 0.50 to 6.50 eV, from bottom to top of each panel ($+0.25$ eV). With the letters A, B and C are indicated the three configurations reported in the text.

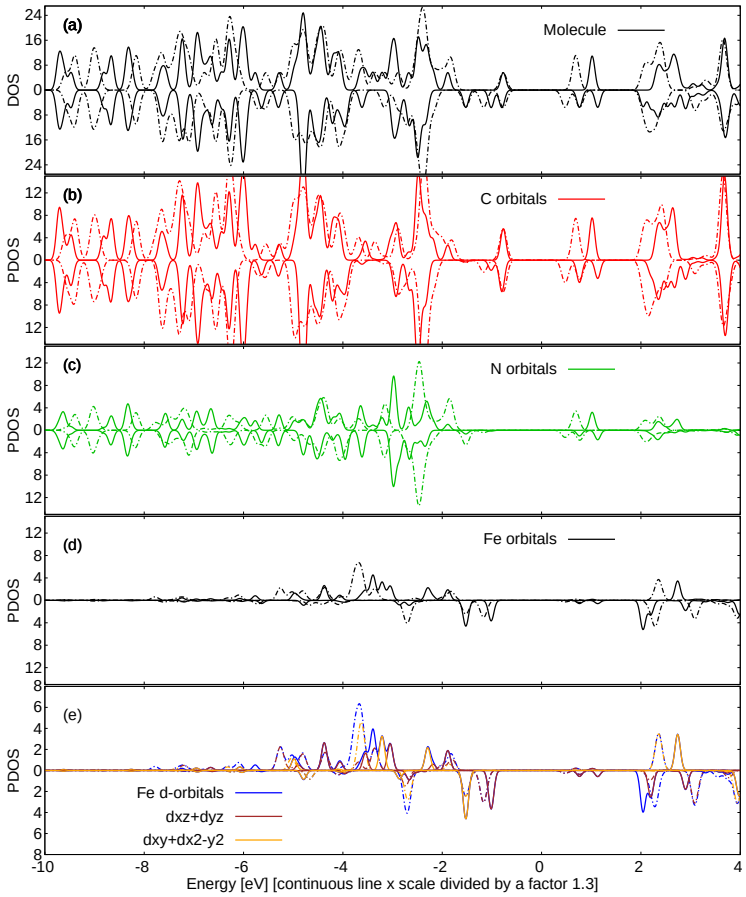

Figure 3.5 DOS of the distorted electronic ground-state configuration of the Fe-phthalocyanine, from a PBE0 calculation (continuous-line) and from a PBE+U (5.00 eV) calculation (dotted-line) is reported in panel (a); the corresponding PDOS over the C atoms, the N atoms and the Fe atom is reported in panels (b), (c) and (d), respectively. The PDOS over the d orbitals of the Fe atom is reported in panel (e). In order to facilitate the comparison, the energy scale of the PBE0 calculation is divided by a factor 1.3 with respect to the energy scale of the PBE+U calculation. The energy scale reported is the one of the PBE+U calculation. IN t

Table 3.4 Löwdin populations of the Fe atom d orbitals of the distorted electronic ground-state configuration of the Fe-phthalocyanine, from a PBE0 calculation and from a PBE+U+VdW (5.00 eV) calculation.

calculation	μ	ρ	dz2	dxz	dyz	dx2-y2	dxy
PBE+U+VdW	2.05	15.79	$\uparrow$ (0.94,0.03)	$\uparrow$ (0.97,0.02)	$\uparrow\downarrow$(0.95,0.90)	(0.36,0.25)	$\uparrow\downarrow$ (0.97,0.96)
PBE0	2.05	14.09	$\uparrow$ (0.96,0.04)	$\uparrow$ (0.98,0.05)	$\uparrow\downarrow$ (0.96,0.87)	(0.36,0.27)	$\uparrow\downarrow$ (0.98,0.97)

Table 3.5 HOMO-LUMO gap in the two spin-channels of the distorted electronic ground-state configuration of the Fe-phthalocyanine, from a PBE0 calculation and from a PBE+U+VdW (5.00 eV) calculation

calculation	spin-up HOMO-LUMO [eV]	spin-down HOMO-LUMO
PBE+U+VdW	1.46	1.25
PBE0	2.32	2.03

apart an energy scale dilatation (1.3 dilatation factor). The HOMO-LUMO gap, as expected, is larger in the calculations with Hybrids xc-functionals than in the one with PBE xc-functionals with VdW and U corrections, as reported in Table 3.5. In fact, the former are better into correcting the self-interaction error and introducing correlation effects, moving the empty states to higher energies.

3.6 Optical spectra

At this point we can consider the spectra of the two calculations reported in Section 3.5 with some differences and some attentions. Due to implementation reasons (YAMBO [125] does not support some DFT parameters as): VdW corrections will be not considered (these corrections do not significantly affect the PDOS), instead of ultra-soft pseudo-potentials norm-conserving pseudo-potentials will be used (these two different kinds of pseudo-potentials give analogue results), and $+U$ corrections will not be taken into account in the commutator of the dielectric function (we verified that this approximation in bulk systems (NiO) gives a difference in the spectra below 10%). Thus, summarizing, we will follow the two numerical routes:

- 1) PBE+U and IPA spectra
- 2) PBE0 and G_0W_0+BSE spectra (one cycle of the GW equations is considered and the corrections added to the energy spectrum before the BSE calculation)

In Fig. 3.6 the 3D polarizability is reported for the two numerical routes. We remind here that the differences between PBE+U calculations and PBE0 calculations have been reported in Section 3.5.

Here, we are mainly interested in the transitions characterizing the first peaks, respectively at $\simeq 1.44$ eV and at 2.07 eV. But first a few remarks about the G_0W_0 correction are needed. The G_0W_0 increases the HOMO-LUMO gap $2.17 \rightarrow 4.39$ eV, and switches the HOMO and the HOMO+1 in the spin-up channel. As already observed the states near Fermi in the PBE+U and PBE0 calculations have the same atomic contributions (as underlined in the PDOS in Fig. 3.5), despite some energy shifts, so when we will refer

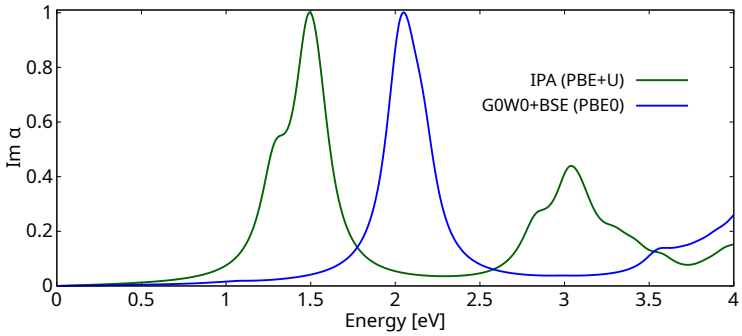

Figure 3.6 Polarizability of the Fe-phthalocyanine normalized in order to have the first peak of the spectrum equal to one: obtained through an IPA calculation (Green line) and a G_0W_0+BSE calculation (Blue line).

to the HOMO and LUMO, LUMO+1 in terms of atomic composition we will not distinguish between the two calculations. The switch of states due to the G_0W_0 cycle, will be considered as part of the "BSE route" and hidden in the transitions analysis, so that there would not be any confusion about the DFT states. The transitions composing the two peaks are reported in Table 3.6 for the different spin-channels. The orbital character of the states appearing in the transitions is reported in Table 3.7

Table 3.6 Transitions involved in the first peak of the polarizability of the Fe-phthalocyanine, obtained through an IPA calculation and a G_0W_0+BSE calculation. The percentage indicates the contribution of the specific transition to the peak.

	Energy (eV)	transition	spin
IPA	1.46	HOMO→LUMO	up
IPA	1.47	HOMO→LUMO+1	up
G_0W_0+BSE	2.07 (20%)	HOMO→LUMO	up
IPA	1.29	HOMO→LUMO	down
IPA	1.53	HOMO→LUMO+1	down
G_0W_0+BSE	2.07 (25%)	HOMO-1→LUMO +1	down
G_0W_0+BSE	2.07 (44%)	HOMO→LUMO+1	down

Looking at the transitions and at the orbital character of the states involved in the transitions, in both cases IPA and G_0W_0+BSE, a movement of charge is expected from the C atoms towards the N atoms and the Fe atom, due to the light excitation. However, the appearance of a transition from a state of mainly Fe character (HOMO-1) underlines as this movement of charge is partially mitigated in the G_0W_0+BSE case. The unbalance between the two spin-channels, is instead larger in the G_0W_0+BSE case.

The similarities between the two cases make us believe that the IPA+U results are sufficiently good for a preliminary analysis of our spinterfaces. In any case, the more accurate BSE approach would be not feasible (computationally) for the same spinterfaces.

Table 3.7 Orbital atomic composition of the states of the DFT+PBE+U+VdW calculation around Fermi for the isolated Fe-phthalocynaine. The results of the DFT+Hybrids calculation are analogue around Fermi apart an energy scale dilatation, as discussed in Section 3.5.

spin channel	state	Fe (%)	C (%)	N (%)
up	HOMO-1	21	58	21
up	HOMO	0	100	0
up	LUMO	2	68	30
up	LUMO+1	2	68	30
down	HOMO-1	42	16	42
down	HOMO	0	100	0
down	LUMO	4	72	24
down	LUMO+1	6	63	31

3.7 Jahn-Teller distorsion

From the preceding sections, from a ground-state perspective, it has emerged the preference of the electronic solution to break the degeneracy of the d states and so the molecular D_{4h} symmetry (the B configuration in Fig. 3.3). In this regard, a detail study of the relation between the electronic solution and the structural geometry is required, also in order to confirm the physical nature of the electronic solution. In order to avoid confusion, we report a few remarks about the numerical setup of this section: we have considered a U value of 5.00 eV [145, 146], VdW xc-functionals [122, 123] and ultrasoft-PP (GBRV) [124].

As a first test (yellow line in Fig. 3.7, leaving N atoms unfixed) we have tried to break the symmetry by moving only a pair of opposite pyrrolic N atoms a certain distance and then leaving them free to structurally relax, together with the rest of the molecule. In Table 3.8 we report the results of this procedure. A small structural deformation is

Table 3.8 Fe-phtalocyanine relaxed structural properties after inducing an initial structural symmetry breaking. Indicated: the initial step Δ_N; the final distance Fe-N along x and y; the difference in energy with respect to the unperturbed structurally and electronically symmetric molecule ΔE; the electronic wavefunction symmetry breaking.

$\Delta_N[10^{-2}$ Å]	Fe-N(x) [Å]	Fe-N(y) [Å]	ΔE [eV]	electronic WF symmetry
0.0	1.93	1.93	0.00	UNBROKEN
0.6	1.94	1.95	-0.62	BROKEN
1.2	1.94	1.93	-0.62	BROKEN
1.8	1.93	1.93	0.00	UNBROKEN

sufficient to obtain the Jahn-Teller deformed configuration. If the initial structural deformation is too large, then the symmetrical configuration is again obtained. As a second test (yellow line in Fig. 3.7, leaving N atoms fixed) let us try to fix the perturbed pair of pyrrolic atoms and let us look at the molecule's structural properties (Table 3.9) and at the Löwdin populations of the Fe atom as well (Table 3.10). We allowed the rest of the molecule to structurally relax. From a structural point of view, it appears how enlarging a pair of pyrrolic-N atoms the other pair follows, until a point ($\Delta_N > 1.2$ Å)

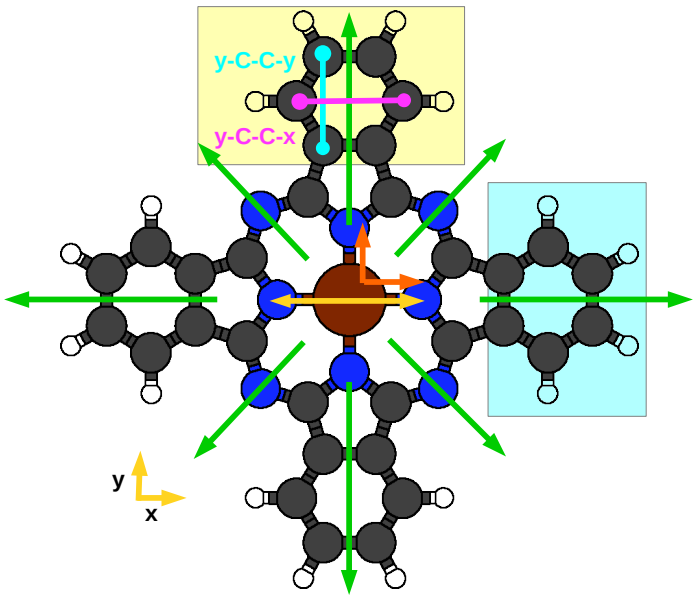

Figure 3.7 Fe-phthalocyanine, where the arrows in green and yellow indicate the different tests considered in the text, while the orange arrows indicate the two Fe-pyrrolic N atoms lengths considered to evaluate the breaking of the D_{4h} symmetry, whose difference is indicated by Δ_N. The light-blue line: C-C distance in the phenyl-ring along y (C-C-y); the purple line: C-C distance in the phenyl-ring along x (C-C-x). The rectangles indicate the different phenyl-rings along and orthogonal to one of the breaking symmetry axis: yellow is the one along the y axis (y-C-C-x,y); blue one is the one along the x axis (x-C-C-x,y).

Table 3.9 Fe-phtalocyanine relaxed structural properties after inducing a structural symmetry breaking (pyrrolic N atoms fixed). Indicated: the fixed step Δ_N; the final distance Fe-N along x and y; the difference in energy with respect to the unperturbed structurally and electronically symmetric molecule ΔE; the a-C-C-b is the C-C distance in the phenyl-rings, with a indicating the molecular axis, while b indicating the bonding considered, as underlined in Fig. 3.2.

$\Delta_N[10^{-2}$ Å]	Fe-N(x) [Å]	Fe-N(y) [Å]	ΔE [eV]	x-C-C-x [Å]	x-C-C-y [Å]	y-C-C-x [Å]	y-C-C-y [Å]
0.0	1.929	1.929	0.000	2.386	2.853	2.386	2.853
0.6	1.935	1.936	-0.620	2.384	2.855	2.382	2.854
1.2	1.941	1.944	-0.622	2.381	2.854	2.382	2.856
1.8	1.947	1.929	0.010	2.383	2.855	2.386	2.855
2.4	1.953	1.935	-0.621	2.381	2.857	2.383	2.854

Table 3.10 Löwdin populations of the Fe atom of relaxed structures after inducing different structural symmetry breaking, keeping the moved pyrrolic N atoms fixed. Indicated: the fixed step Δ_N; the final distance Fe-N along x and y; the difference in energy with respect to the unperturbed structurally and electronically symmetric molecule ΔE.

$\Delta_N[10^{-2}$ Å]	d	dz2	dxz	dyz	dx2-y2	dxy
0.0	(4.34,1.87)	(0.96,0.03)	(0.98,0.30)	(0.98,0.30)	(0.45,0.28)	(0.97,0.96)
0.6	(4.20,2.16)	(0.94,0.03)	(0.95,0.89)	(0.97,0.03)	(0.37,0.25)	(0.97,0.96)
1.2	(4.19,2.15)	(0.94,0.03)	(0.97,0.02)	(0.95,0.90)	(0.36,0.24)	(0.97,0.96)
1.8	(4.36,1.87)	(0.96,0.03)	(0.98,0.30)	(0.98,0.30)	(0.46,0.28)	(0.98,0.96)
2.4	(4.19,2.15)	(0.94,0.03)	(0.95,0.90)	(0.97,0.02)	(0.36,0.24)	(0.97,0.96)

where the following pair try to counterbalance the structural deformation, shortening. From the point of view of the phenyl rings, the C-C distances remain almost unchanged for the different deformations. Looking at the Fe d populations, it is clear how only in certain intervals the symmetry breaking is naturally obtained. In other words, it seems not sufficient to induce a structural symmetry breaking to obtain a symmetry broken wavefunction.

As a third test (green lines in Fig. 3.7) we have deformed the molecule moving each atom by the same quantity along the green lines in Fig. 3.7, and fixed a pair of pyrrolic N atoms, to be sure that the lowering of the energy in the above cases is not due to the major distance between the Fe and the pyrrolic N atoms, and that the molecule prefers to reduce the Fe-N distance than to maintain the symmetry.

The phenyl rings tend to maintain the same form (Table 3.11) as already observed above. Still only for certain Fe-N distances the symmetry broken configuration is naturally obtained. The difference in the relaxation scheme, makes some configurations that were unstable stable and vice-versa; but this is mainly related to the nature of the electronic configuration.

Finally, let us consider the symmetry broken one and let us relax it, this will be our reference configuration for the rest of the thesis, and we will call it the Jahn-Teller configuration. Then in order to be sure that the structural deformation is needed, let us consider a relaxation on the symmetric structure with the broken wave-function. As expected the preferred configuration is the one we called above B. The results are summerized by the Table 3.12. Moreover, we report the PDOS of the two configurations with minimal energy in Fig. 3.8.

Table 3.11 Volumic deformation fixing one pair of pyrrolic N atoms. Indicated: the fixed step Δ_N; the final distance Fe-N along x and y; the difference in energy with respect to the unperturbed structurally and electronically symmetric molecule ΔE; the a-C-C-b is the C-C distance in the phenyl-rings, with a indicating the molecular axis, while b indicating the bonding considered, as underlined in Fig. 3.2.

$\Delta_N[10^{-2}$ Å]	Fe-N(x) [Å]	Fe-N(y) [Å]	ΔE [eV]	x-C-C-x [Å]	x-C-C-y [Å]	y-C-C-x [Å]	y-C-C-y [Å]	WF
0	1.929	1.929	0.000	2.386	2.853	2.386	2.853	Sym
1.2	1.941	1.931	0.003	2.382	2.858	2.384	2.855	Sym
1.8	1.947	1.943	-0.621	2.382	2.856	2.382	2.857	Asym
2.4	1.953	1.923	0.013	2.382	2.857	2.384	2.854	Sym

Table 3.12 FePc isolated molecule, minimal energy configurations: two symmetrical configurations (Symm A and Symm C) and the Jahn-Teller (JT) one configuration. The pyrrolic N pair atoms distances, the energy differences with respect to the symmetrical configuration, the Fe d-orbital populations are reported for each configuration.

	Fe-pyrrolic N+Δ_N [Å]	ΔE [eV]	dz2	dxz	dyz	dx2-y2	dxy
Symm A	1.929 + 0.000	0.000	(0.96,0.03)	(0.98,0.30)	(0.98,0.30)	(0.45,0.28)	(0.97,0.96)
Symm C	1.937 + 0.000	-0.372	(0.94,0.02)	(0.95,0.89)	(0.95,0.89)	(0.41,0.27)	(0.98,0.00)
JT	1.944 + 0.006	-0.623	(0.94,0.03)	(0.97,0.02)	(0.95,0.90)	(0.36,0.25)	(0.97,0.96)

3.8 Spin crossover

The Fe-phthalocyanine is known to be a spin-crossover molecule [87, 148, 149]. To understand how much energy is indeed needed to switch its spin state LOW→HIGH, we did a calculation imposing as starting condition a higher magnetic moment of the Fe atom ($+2\mu_B \rightarrow +4\mu_B$). These are calculations on the D_{2h} structural geometry, with a PBE+U+VdW setup and ultrasoft pseudo-potentials (GBRV). In Table 3.13, the two spin configurations are reported. Their respective PDOS is instead reported in Fig. 3.9.

Table 3.13 Löwdin populations of the Fe atom before and after spin-crossover excitation.

Spin State	μ [μ_B]	ρ	ΔE [eV]	dz2	dxz	dyz	dx2-y2	dxy
LOW	2.05	15.79	0.00	(0.94,0.03)	(0.97,0.02)	(0.95,0.90)	(0.36,0.25)	(0.97,0.96)
HIGH	3.68	15.66	0.46	(0.95,0.90)	(0.98,0.02)	(0.98,0.02)	(0.99,0.24)	(0.98,0.01)

From the perspective of the Fe population, as reported in the Table 3.13, in the spin-crossover transition the $d_{z2}\downarrow$, the $d_{xy}\downarrow$ and the $d_{x2-y2}\uparrow$ are filled while the $d_{yz}\downarrow$ is emptied. The charge on the Fe atom does not increase, so the charge redistribution is mainly taking part between the Fe p and d orbitals. The electronic configuration reacquires a D_{4h} symmetry, so we expect the spin-crossover transition to be accompanied by a slight structural readjustment. From the perspective of the PDOS 3.9, the deep states are untouched by the transition, apart some modifications at $\simeq -6$ eV in the C atoms states. Near Fermi a few modifications occur on the N and C atoms states. An interesting feature is the C atom peak slightly above Fermi, which reacquires its degeneracy; probably due to the fact that the molecule after the spin-crossover transition does not need to Jahn-Teller distort anymore.

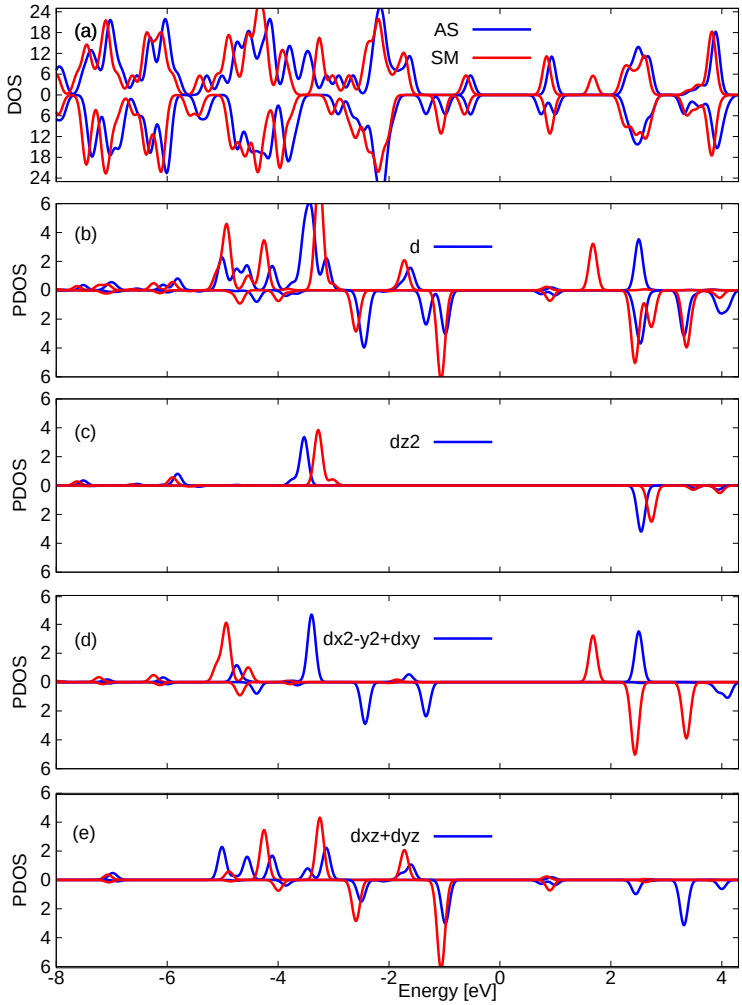

Figure 3.8 DOS (a) and PDOS (b-e) of the two electronic configurations of the Fe-phthalocyanine, the one preserving the symmetry D_{4h} (SM) and the one breaking it (AS). Color scheme as follows: Blue: AS; Red: SM. In the PDOS panels (b-e) the projections of the DOS over the d orbitals of the Fe atom are reported.

3.9 Magnetic and charge configurations

We report the charge and magnetic configurations of the JT configuration in Fig. 3.10. The Jahn-Teller distorsion is underlined not only by the electronic filling of the Fe d orbitals, but also by the distribution of the magnetic moments in the molecule. An interesting feature of the magnetic moments ordering is the opposite direction of the N atoms magnetic moments with respect to the Fe atom magnetic moment; this characteristic will be considered in the explanation of some of the spinterfaces adsorption configurations energies. The relevance of the N atoms as of the Fe atom in the spinterfaces studies of the following chapters is partially suggested by their significant magnetic contribution

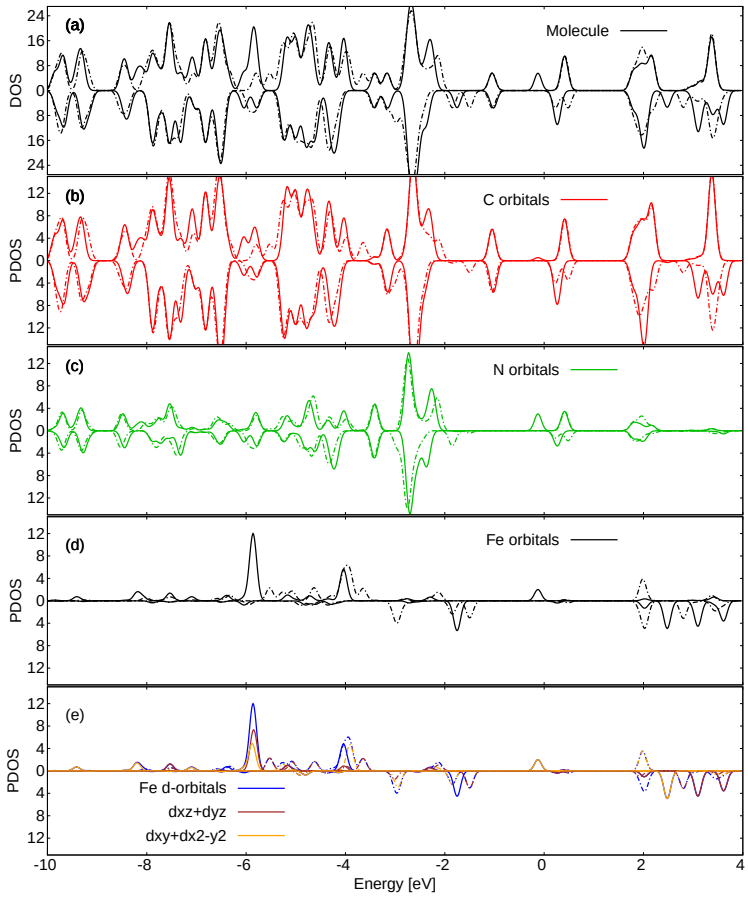

Figure 3.9 DOS (a) and PDOS (b-e) of the two electronic configurations of the Fe-phthalocyanine, the ground state one (dotted-line) and the spin-crossover one (continuous-line). In the PDOS panels (b) and (c), the projections of the DOS over the C atoms and N atoms orbitals are respectively reported. In the PDOS panel (d) the projection of the DOS over the Fe orbitals is reported. The different d orbitals contributions are instead reported in panel (e).

and charge contribution to the molecule.

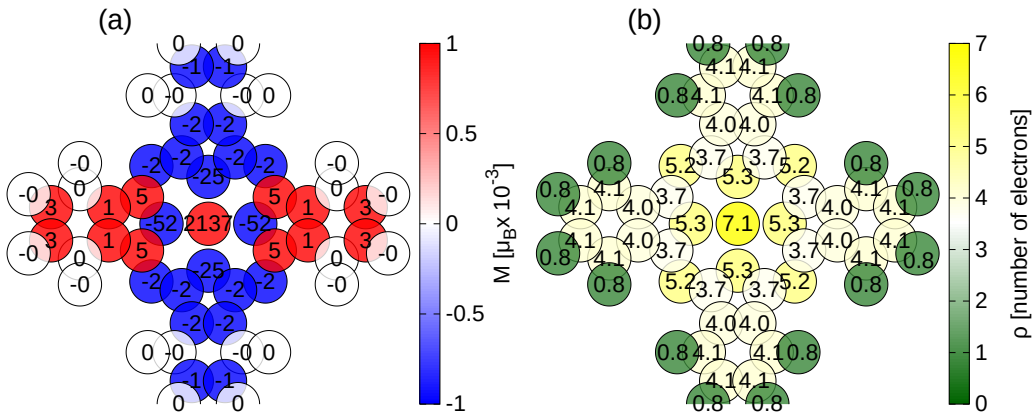

Figure 3.10 (a) magnetic moments and (b) electronic populations of the different atoms of the molecule, extracted from the Löwdin populations. In the case of the magnetic moments the two colors (Red and Blue) represent a different direction, while in the case of the electronic populations, a major (yellow) contribution of electrons to the atom.

Part III
Fe-phthalocyanine on CoO

CHAPTER 4

Fe-phthalocyanine on CoO(001)

In this chapter we study the FePc/CoO(001) spinterface from an energetic, magnetic and optical point of view. Among the different adsorption configurations of the molecule on the substrate the minimal adsorption energy configuration is the one with the Fe atom over the O atom and the molecule partially rotated. The adsorption of the molecule produces modifications in the O atoms all over the surface, while only the Co atoms underneath the molecule are affected. This suggests some spatial long-range interaction between the molecule and the substrate, mainly involving the O orbitals and so pointing to some itinerant magnetism effect.

4.1 Computational details

Cobalt monoxide in FCC structure, is a Mott insulator, which shows antiferromagnetic ordering for temperature below the Nèel temperature of 289 K. Not only it has a significant orbital magnetic moment [150], but it also shows a monoclinic Jahn-Teller distortion due to the partial filling of the t_{2g} orbitals [151]. In the surface CoO(001) system, the reduced symmetry ($O_h \rightarrow D_4$) implies a partial filling of the e_g orbitals, due to their hybridization with the t_{2g} orbitals. The use of PBE xc-function with U+VdW corrections gives a lower magnetic moment ($\simeq 2.6\mu_B$) than the one reported from analogue bulk calculations without U+VdW corrections ($\simeq 2.7\mu_B$) [151], despite an increase at the surface would be expected.

We evaluate the ground state of the FePc/CoO(001) spinterface and its properties using DFT in a plane-wave basis set, with U and VdW corrections, as already pointed out in the Section 2.4. The values considered, $U_{Co} = 4.0$ eV and $U_{Fe} = 5.0$ eV, were chosen following the literature so as to reproduce the experimental electronic properties (density of states) of the localized orbitals for the isolated systems [12, 119]. Note, however, with these values, the CoO spin momentum is underestimated, while the magnetism of the Fe atom of the molecule is well reproduced. The substrate is modeled with a slab that includes 3 CoO layers. Equilibrium geometries are obtained through a structural optimization of the molecule and of the top two layers of the substrate. In the same way, the optical spectra are obtained and analyzed following what already pointed out in Section 2.4.

4.2 Adsorption configurations

The adsorption of FePc on CoO(001) is studied considering the surface supercell with the epitaxy matrix $((6,0)(3,3))$, built from the surface magnetic unit cell, as depicted in Fig. 4.1.

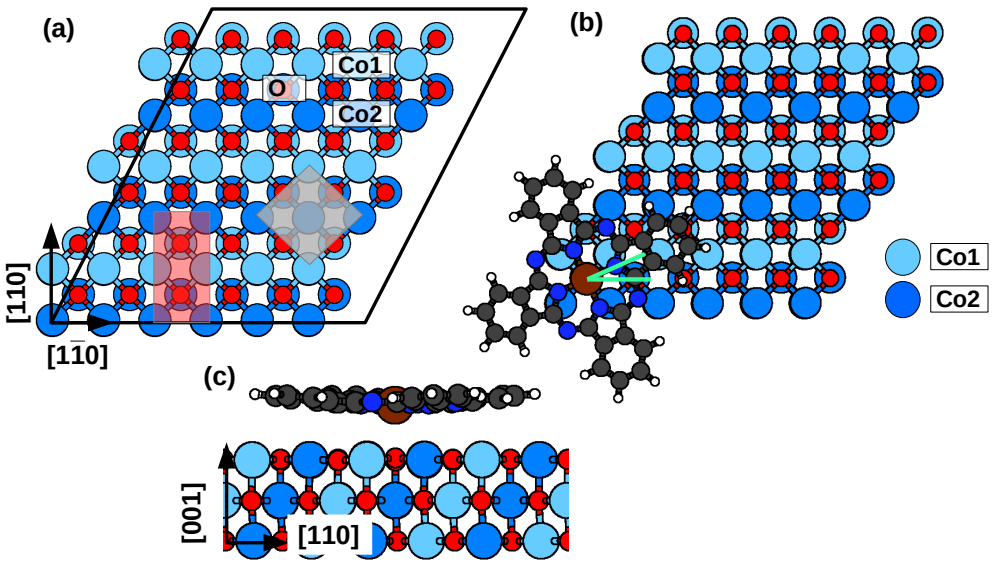

Figure 4.1 (a) surface supercell adopted for the calculations (black line), having epitaxy matrix $((6,0)(3,3))$ with respect to the surface primitive cell of antiferromagnetic CoO(001) (shaded-grey); (b) adsorption configuration from a top-view, with the considered molecular angle in water-green; and (c) adsorption configuration from a side-view. Color scheme as follows. Light and dark blue: Co atoms, according to their magnetization; Red: O; Brown: Fe; Blue: N; Dark-gray: C; Light-gray: H.

Different adsorption configurations have been considered, these are distinguished by the adsorption center under the Fe atom, i.e. Co or O, the molecular orientation, i.e. the angle between one of the molecule axis N-Fe-N and the substrate crystalline direction $[1\bar{1}0]$, and the Fe atom magnetic orientation with respect to the Co one underneath (in case of the O adsorption the Co considered is the one under the O atom). The ferromagnetic (FM) configuration is the one with the two magnetic moments parallel, while the antiferromagnetic (AF) is the one with the two anti-parallel. The optimized structures are reported in Fig. 4.2. The adsorption energies of the different configurations, instead, are reported in Table 4.1.

In the O configurations at angles greater than 0° lower adsorption energies, i.e. stronger binding between the molecule and the substrate, shorter distances of the molecule from the substrate and a different bending concavity of the molecule are observed with respect to the Co configurations. In particular, in the Co configurations, the Fe atom is in a range of $3.31 - 3.38$ Å with respect to the top surface of the substrate, having partially dragged the N atoms in a range of $3.29 - 3.37$ Å, and the C atoms are in a range of $3.21 - 3.33$ Å. In the O configurations, instead, the Fe atom is in a range of $2.86 - 3.12$ Å, having dragged now the N atoms in a range of $2.99 - 3.18$ Å, and the C atoms are in a range of $3.12 - 3.19$ Å. Thus, the molecule, as former said, is lower and has a negative concavity over the O atoms, while is higher and has a positive concavity over the Co atoms. This bending is maximum at 22° in the Co configuration and at 24° in the

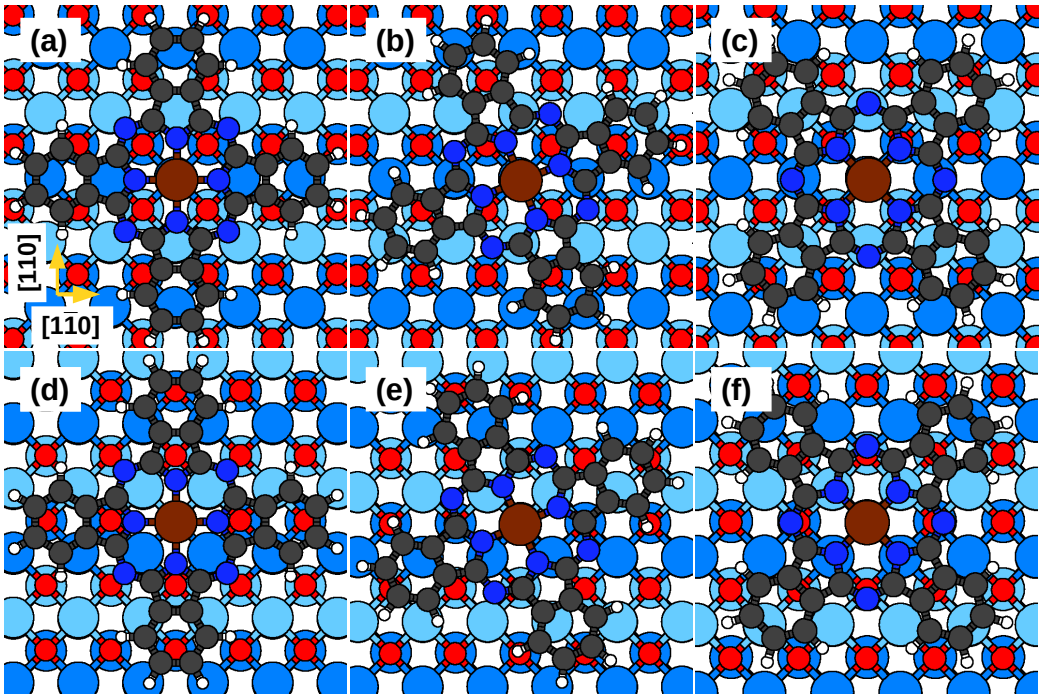

Figure 4.2 Optimized geometries for FePc/CoO(001) for the adsorption configurations considered: on a Co1 site at $0°$ (**a**), at $22°$ (**b**), at $45°$ (**c**), on a O site at $0°$ (**d**), at $24°$ (**e**) and at $45°$ (**f**). The color scheme is the same as in Figure 4.1

Table 4.1 Adsorption energy for FePc/CoO(001) as a function of adsorption site and optimized angle, for FM and AF orientation of the Fe spin with respect to underlying Co. Values in eV.

Site	Angle	E_{ads}^{FM}	E_{ads}^{AF}	$E_{ads}^{AF} - E_{ads}^{FM}$
Co	$0°$	-3.742	-4.441	-0.698
Co	$22°$	-3.563	-4.209	-0.646
Co	$45°$	-4.320	-4.211	0.108
O	$0°$	-3.466	unstable	
O	$24°$	-4.693	-4.700	-0.008
O	$45°$	-4.618	-3.720	0.898

O one. The bending of the molecule, could be then related to the increase or decrease of the adsorption energy, looking at Table 4.1. However, this is not sufficient to explain the variations in the adsorption energies at some angles (i.e. O at $0°$) and magnetic configurations (i.e. AF O at $45°$); in fact, the bending difference between the two magnetic configurations Co FM and Co AF is too small to be significant $\simeq 1 \times 10^{-3}$ Å.

The position of the pyrrolic and imide N atoms seems as relevant as the bending, in terms of adsorption energy and magnetic configuration. For instance, in the O con-

figuration at 0° (see Fig. 4.2-(d)), the imide N atoms are positioned close to O atoms of the substrate which are above equally magnetized Co atoms, acquiring due to super-exchange an anti-parallel magnetization with respect to the Co atoms. Because the Fe atom tends in the isolated molecule to be magnetized anti-parallel with respect to the N atoms, to "impose" in the adsorbed configuration the Fe atom magnetization parallel to the one of the N atoms, makes the adsorbed configuration higher in energy than the un-adsorbed one. Analogously, the symmetrical positioning of the N atoms in the O configuration at 24° (see Fig. 4.2-(e)), makes the ordering of their magnetic moment not-binding for the Fe atom, which instead is affected by the super-exchange coupling with the Co underneath. In the case of the Co configuration at 0° (see Fig. 4.2-(a)) the imide N atoms are again relevant: coupling directly with the Co atoms underneath, acquiring all a parallel magnetization and favouring an anti-parallel magnetization of the Fe, which is now parallel with respect to the Co underneath.

The same can be said for the pyrrolic N atoms, as in the case of the Co configurations at 0° and 22° (see Fig. 4.2-(a) and (b)).

The Co configuration at 45°, due to symmetrical positioning of the N atoms, should behave as the O configuration at 45°, favouring the Fe coupling with the atom underneath. However, instead of a ferromagnetic coupling an anti-ferromagnetic one is found. However, in this case the Fe atom is nearer a pair of imide N atoms equally magnetized with respect to the other (0.4×10^{-3} Å). This suggests also in this case, how the magnetic bonding Fe-N is much more relevant than the Fe-atom underneath bonding.

The relevance of the N atoms magnetic ordering in defining the molecule magnetic configuration and the adsorption energy can be an hint of the relevance of the itinerant magnetism in this spinterface (look below).

4.3 Electronic properties

The minimum adsorption configuration is the O one at 24°, with magnetic ordering AF with respect to the Co2 underneath the O atom. We investigate its electronic properties, looking at the PDOS in Fig. 4.3. The molecular LUMO is inside the conduction-valence gap of the substrate, so that the conduction-valence gap of the entire system is reduced: in the spin-up channel from 1.60 eV to 0.97 eV, while in the spin-down channel from 1.60 eV to 0.85 eV. The molecular HOMO, instead, partially hybridizes with the valence levels of the substrate ($1 - 2\%$).

Generally, the molecular levels are significantly affected by the adsorption: a large spreading of the levels at 2.0 eV and $\simeq 5$ eV below the Fermi energy can be observed. The Fe d orbitals pointing towards the surface as the $dz2$ and $dxz + dyz$ are the ones most affected, underlining a strong directional hybridization between the molecule and the substrate. The only exceptions are the HOMO-LUMO levels and the deep molecular states, which instead are almost untouched.

The substrate levels are as well quite modified during the adsorption. The de-localized nature of the states, due to the O contribution, probably makes them particularly susceptible to external perturbations.

4.4 Magnetic properties

At this point we can study the magnetic properties of the spinterface looking at its spin variations and electronic charge variations after adsorption, as reported in Fig. 4.4. But first it is necessary to remind how the GGA+U results underestimate the Co magnetic

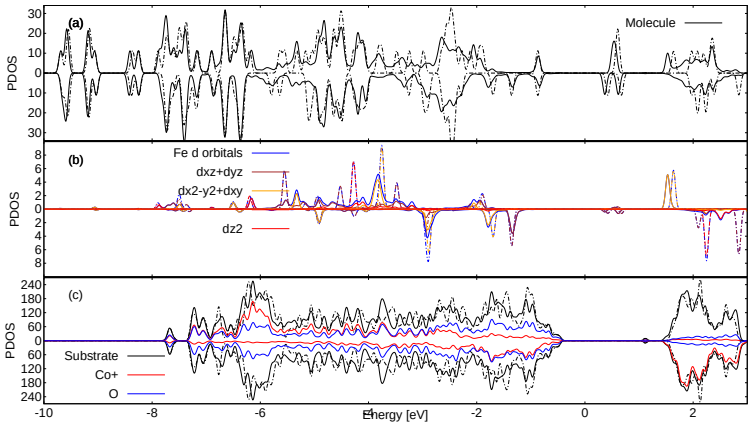

Figure 4.3 Electronic PDOS of FePc/CoO(001), summed over: (a) all molecule atoms; (b) Fe d-orbitals; (c) substrate atoms. Substrate color codes: black = all substrate atoms; red = Co atoms of one spin component ("Co+", d orbitals); blue = all O atoms. Solid/dash-dotted lines indicate adsorbed and gas phase molecules or pristine substrate, respectively. Negative spin components are shown as negative values. All values in states/eV/cell. The majority spin-channel HOMO states of the molecule, the one related to the isolated molecule and the one related to the adsorbed one, are aligned.

moments in the bulk system, even when orbital contributions are considered [151]. In our case, the magnetic moments of the Co atoms at the surface are of $\simeq 2.60\mu_B$ (while those in the internal layer are of $\simeq 2.56\mu_B$), still quite lower than the expected bulk-like ones, in spite in the substrate top-layers an increase would be likely.

The fact that the main magnetic variations are on the O atoms ($\simeq 33 \times 10^{-3}\mu_B$) and all over the surface, and that these are not strictly related to electronic population variations, underlines the itinerant nature of the substrate magnetism. This could also explain the large number of magnetic configurations we encountered while optimizing the electronic structure of CoO(001).

Looking at Fig. 4.4-(a) partial modifications of the magnetic moments of the Co atoms ($\simeq 10 \times 10^{-3}\mu_B$) in proximity of the molecule Fe center can be observed. These modifications, correlate to modifications in the electronic density in Fig. 4.4, as expected by the localized nature of the magnetism of the transition-metal atoms. Thus this spinterface shows both kind of magnetisms: localized and itinerant.

From a side-view in Fig. 4.4 (e)-(f), it becomes apparent how the interaction between the molecule and the substrate is mainly localized at the interface, with a deeper interaction under the Fe center. This propagation is the sign of a super-exchange coupling through a superficial O between the Fe atom and the Co underneath (whose magnetic moment increases by $6 \times 10^{-3}\mu_B$) in the middle layer.

Looking at the molecule in Fig. 4.4 (b) and (d), the magnetic variations are seen at the atoms in the center, while the electronic charge ones can also be seen in the atoms of the phenyl-rings.

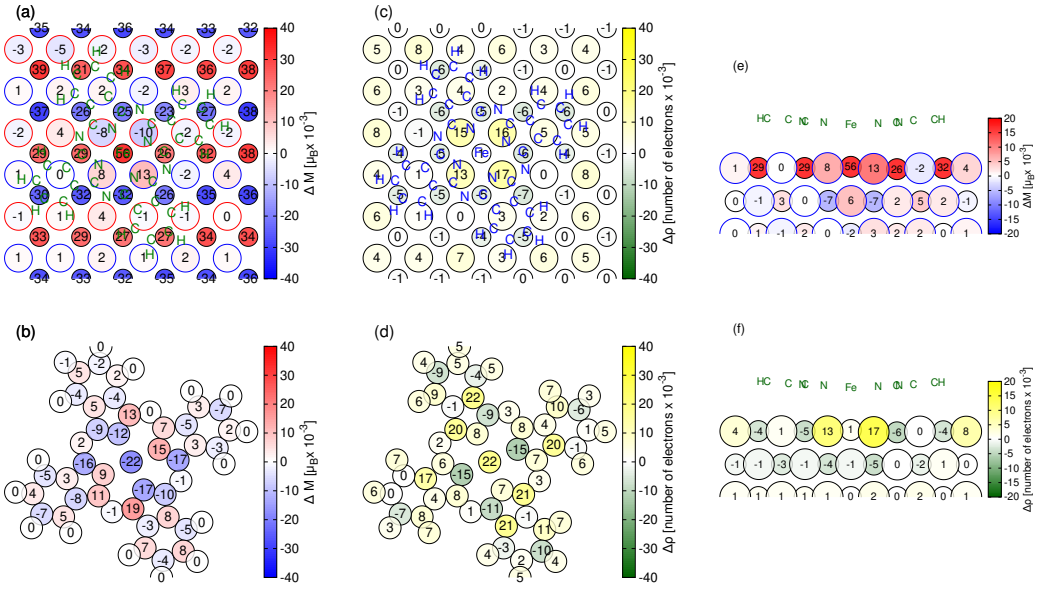

Figure 4.4 Variations in the atomic magnetic moments for FePc/CoO(001), seen from top, with respect to the isolated systems, on (a) the surface and on the molecule (b). Corresponding variations in the electronic density (c) and (d). (positive = increase in electron population). Side view of the variations: (e) magnetic moments and (f) charge density. The positions of the molecule atoms are marked by green/blue letters in panels (a), (c), (e) and (f). Notice that few values in the plot exceed the maximum ones of the scale bar.

4.5 Optical properties

At this point, we can discuss the optical properties of the spinterface FePc/CoO(001) in its minimum adsorption configuration, reporting the $2D$ polarizability in Fig. 4.5, for the adsorbed system and for the pristine one. The intensities of the three spectra are scaled by the same factor, chosen so to normalize to unity the transition at $\simeq 1.5$ eV in the free molecule. In the upper inset of Fig. 4.5, the molecular contributions (yellow) to the valence and conduction states $P_b^{(v/c)}$ are reported for each bin of transitions (purple). The corresponding spin channel of the bin of transitions (b) is reported in the lower inset of Fig. 4.5, with its intensity normalized to the one of the highest bin in the spin channel. These quantities have been introduced in the Section 2.4.2.

The different transitions at the lowest part of the spectrum have equal compositions and intensities: valence states of substrate nature and conduction ones of molecular nature. This underlines a charge movement from the substrate to the molecule as a consequence of the light excitation. A partial spin asymmetry of the transitions, moreover, can suggest a spin selection in the charge movement. In case of opposite magnetization of the molecule we would expect opposite spin selection. However, let us note that the energy difference between the two spinterface molecular magnetizations, AF and FM, is too small ($\simeq 8 \times 10^{-3}$ meV) to realistically expect the formation of a ferromagnetic layer of spinterfaces in an experimental situation, or to produce a net spin current through

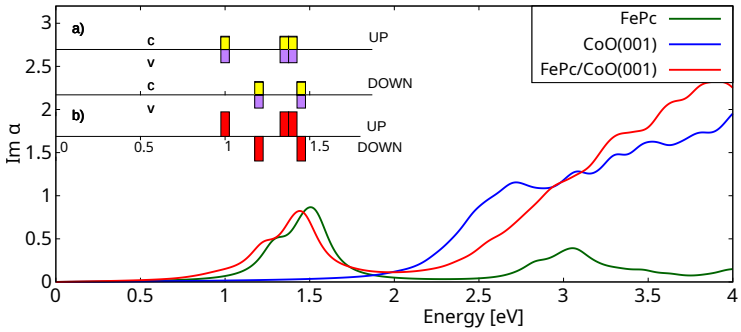

Figure 4.5 Optical absorption spectra (independent particle): polarizability of CoO(001) (blue), FePc/CoO(001) (red), and an FePc molecular layer such as in FePc/CoO(001) (green). The arbitrary units of Im α are chosen by normalizing the molecular peak at $\simeq$1.5 eV (green line) to 1. The transitions are broadened by 0.05 eV. Bottom inset (b): the intensities (red) of the main transitions contributing to the FePc/CoO(001) spectrum in the spin-up (top) and spin-down (bottom) channels, normalized with respect to the largest one at $\simeq$1.4 eV. Only values greater than 5% are shown. Top inset (a): the percentage of projection of the respective valence(bottom)/conduction(top) level on the molecule (yellow), characterizing the main transitions.

light excitation over large areas ($\simeq 100$ Å).

Calculating the relative heights of the valence and conduction states of the transitions, we have $z_c = 0$ Å at the same height of the Fe atom, underneath the molecule, while $z_v \simeq -7$ Å in the spin-up channel at the bottom layer, and in the spin-down channel between the bottom and the middle layer $z_v \simeq [-5, -7]$ Å. These results confirm a movement of charge from the substrate towards the molecule after the light excitation, as deduced above by the nature of the conduction/valence states of the transitions.

4.6 Conclusions

We have here studied the FePc/CoO(001) spinterface. The molecule adsorbs on the O atom, with its molecular axis partially rotated with respect to the crystalline ones. The interface presents peculiar characteristics: on one hand, localized modifications of the magnetism of Co atoms in proximity of the Fe atom, and associated charge variations; on the other hand, modifications all over the surface of the magnetism of the O atoms, and no charge variations directly associated to them. We suppose that, while the former phenomena are directly related to local magnetism effects, the latter are due to some itinerant magnetism effect instead. We suppose that this interface could be very interesting from the perspective of the mixed itinerant and localized magnetism, but, due to the former, inappropriate to be externally manipulated, because of its high perturbability.

For what concern the charge variations observed at the interface the following statement can be done. In the adsorption there is an accumulation of charge at the interface. This charge from the C atoms (HOMO) of the molecule saturates the O atoms of the surface (the valence state at the surface is of O nature). The charge which was shared in the pristine substrate between the O atoms and the transition-metal atoms is then released

back to the transition-metal atoms due to the saturation of the O atoms after adsorption. The reduction observed on the O atoms is then due to the fact that the spilling charge at the pristine interface, is now majorly projected on the de-localized states of the molecule.